

This is an Open Access document downloaded from ORCA, Cardiff University's institutional repository: <https://orca.cardiff.ac.uk/id/eprint/132757/>

This is the author's version of a work that was submitted to / accepted for publication.

Citation for final published version:

Fan, Yaoshen, Chen, Shenliang, Pan, Shunqi and Dou, Shentang 2020. Storm-induced hydrodynamic changes and seabed erosion in the littoral area of Yellow River Delta: a model-guided mechanism study. *Continental Shelf Research* 205 , 104171. 10.1016/j.csr.2020.104171

Publishers page: <http://dx.doi.org/10.1016/j.csr.2020.104171>

Please note:

Changes made as a result of publishing processes such as copy-editing, formatting and page numbers may not be reflected in this version. For the definitive version of this publication, please refer to the published source. You are advised to consult the publisher's version if you wish to cite this paper.

This version is being made available in accordance with publisher policies. See <http://orca.cf.ac.uk/policies.html> for usage policies. Copyright and moral rights for publications made available in ORCA are retained by the copyright holders.



# Journal Pre-proof

Storm-induced hydrodynamic changes and seabed erosion in the littoral area of Yellow River Delta: A model-guided mechanism study

Yaoshen Fan, Shenliang Chen, Shunqi Pan, Shentang Dou



PII: S0278-4343(20)30127-8

DOI: <https://doi.org/10.1016/j.csr.2020.104171>

Reference: CSR 104171

To appear in: *Continental Shelf Research*

Received Date: 27 January 2020

Revised Date: 26 May 2020

Accepted Date: 28 May 2020

Please cite this article as: Fan, Y., Chen, S., Pan, S., Dou, S., Storm-induced hydrodynamic changes and seabed erosion in the littoral area of Yellow River Delta: A model-guided mechanism study, *Continental Shelf Research* (2020), doi: <https://doi.org/10.1016/j.csr.2020.104171>.

This is a PDF file of an article that has undergone enhancements after acceptance, such as the addition of a cover page and metadata, and formatting for readability, but it is not yet the definitive version of record. This version will undergo additional copyediting, typesetting and review before it is published in its final form, but we are providing this version to give early visibility of the article. Please note that, during the production process, errors may be discovered which could affect the content, and all legal disclaimers that apply to the journal pertain.

© 2020 Published by Elsevier Ltd.

1 **Storm-induced hydrodynamic changes and seabed erosion in**  
2 **the littoral area of Yellow River Delta: A model-guided**  
3 **mechanism study**

4 Yaoshen Fan <sup>a,c</sup>, Shenliang Chen <sup>a,\*</sup>, Shunqi Pan <sup>b,a</sup>, Shentang Dou <sup>c</sup>

5 <sup>a</sup> *State Key Laboratory of Estuarine and Coastal Research, East China Normal University,*  
6 *Shanghai 200241, China;*

7 <sup>b</sup> *Hydro-environmental Research Centre, School of Engineering, Cardiff University, Cardiff CF24*  
8 *3AA, UK;*

9 <sup>c</sup> *Yellow River Institute of Hydraulic Research, Yellow River Conservancy Commission,*  
10 *Zhengzhou 450003, China*

11 \*Corresponding author.

12 Tel: 021-54836498; Email address: [slchen@sklec.ecnu.edu.cn](mailto:slchen@sklec.ecnu.edu.cn) (S.L. Chen)

13 **Highlights**

- 14 • Storm-induced energetic hydrodynamic forces intensify sediment  
15 resuspension and dispersal significantly.
- 16 • Wave-induced bottom stress promotes sediment plume and enhances local  
17 resuspension.
- 18 • Storms increase suspended sediment concentration and offshore sediment  
19 transport.
- 20 • Storm-induced accumulative effect on seabed scour tends to cause long-term  
21 erosion.

**22 Abstract**

23 Morphological evolution of large river deltas is highly vulnerable to extreme  
24 storm events due to insufficient sediment supply. As an abandoned delta lobe, the  
25 coasts along the northern Yellow River Delta (YRD) and Gudong Oil Field have  
26 recently suffered serious erosion due to extreme storm events and become  
27 increasingly vulnerable. In this study, a well validated and tested Delft 3D module by  
28 the observing hydrodynamic and sediment data to simulate the hydrodynamics and  
29 seabed erosion during a storm event in the littoral area of YRD. Observed wave,  
30 current and sediment data under both fair-weather and storm conditions were  
31 collected in the study area and used to validate the model. The results indicated that  
32 the model can reproduce well the hydrodynamic and sediment transport processes. A  
33 series of numerical experiments were carried out to examine the hydrodynamic  
34 changes and sediment transports. In the numerical experiment of normal condition,  
35 there is hardly any sediment transport off the YRD. The numerical experiment of  
36 storm condition showed that storms enhanced tidal residual currents, weakened tidal  
37 shear front, and significant wave heights up to 2 m, considerably intensified the  
38 sediment resuspension and dispersal. The local sediment resuspension due to the  
39 increased wave-induced bottom stress promoted the sediment plume to expand to the  
40 central area of Laizhou Bay, which seemed to provide sediment source for offshore  
41 and southward transport. During the storm, the active nearshore sediment  
42 resuspension provided sediment source for offshore and southward transport. The  
43 intensive dynamics and sediment transport under storm conditions caused significant

44 changes in seabed erosion and siltation. The main erosion occurred off the Gudong  
45 and northern YRD, while the main siltation appeared in the central area of Laizhou  
46 Bay. No significant recovery after a storm and frequent strong winds have an  
47 accumulative effect on the erosion, which is very likely to dominate the erosive states  
48 of the YRD coast in the future.

49 **Keywords:** Yellow River Delta; Storms; Tidal shear front; Sediment transport;  
50 Seabed erosion; Morphodynamics

## 51 **1 Introduction**

52 Fluvial discharge, wave energy and tidal range are critical in determining  
53 morphological evolutions of most deltas worldwide. Sediment input to deltas has been  
54 reduced or eliminated (Syvitski and Kettner, 2011; Wang et al., 2011; Dai et al., 2016;  
55 Liu et al., 2019), which causes delta erosion and sinking, and increasing delta's  
56 wetlands will be drowned (Tessler et al., 2015; Wolters and Kuenzer, 2015; Murray et  
57 al., 2019). Lack of knowledge on erosion mechanism and deltaic processes may lead  
58 to erroneous conclusions about how deltas function. More recently, sea level rise,  
59 insufficient supply of sediment, human interventions and climate changes, which may  
60 cause more extreme event, such as flood and storm have been the emerging key  
61 factors to reshape mega-deltas (Nicholls and Cazenave, 2010; Blum and Roberts 2009;  
62 Yang et al., 2011a; Bi et al., 2014; Liu et al., 2017; Becker., 2020).

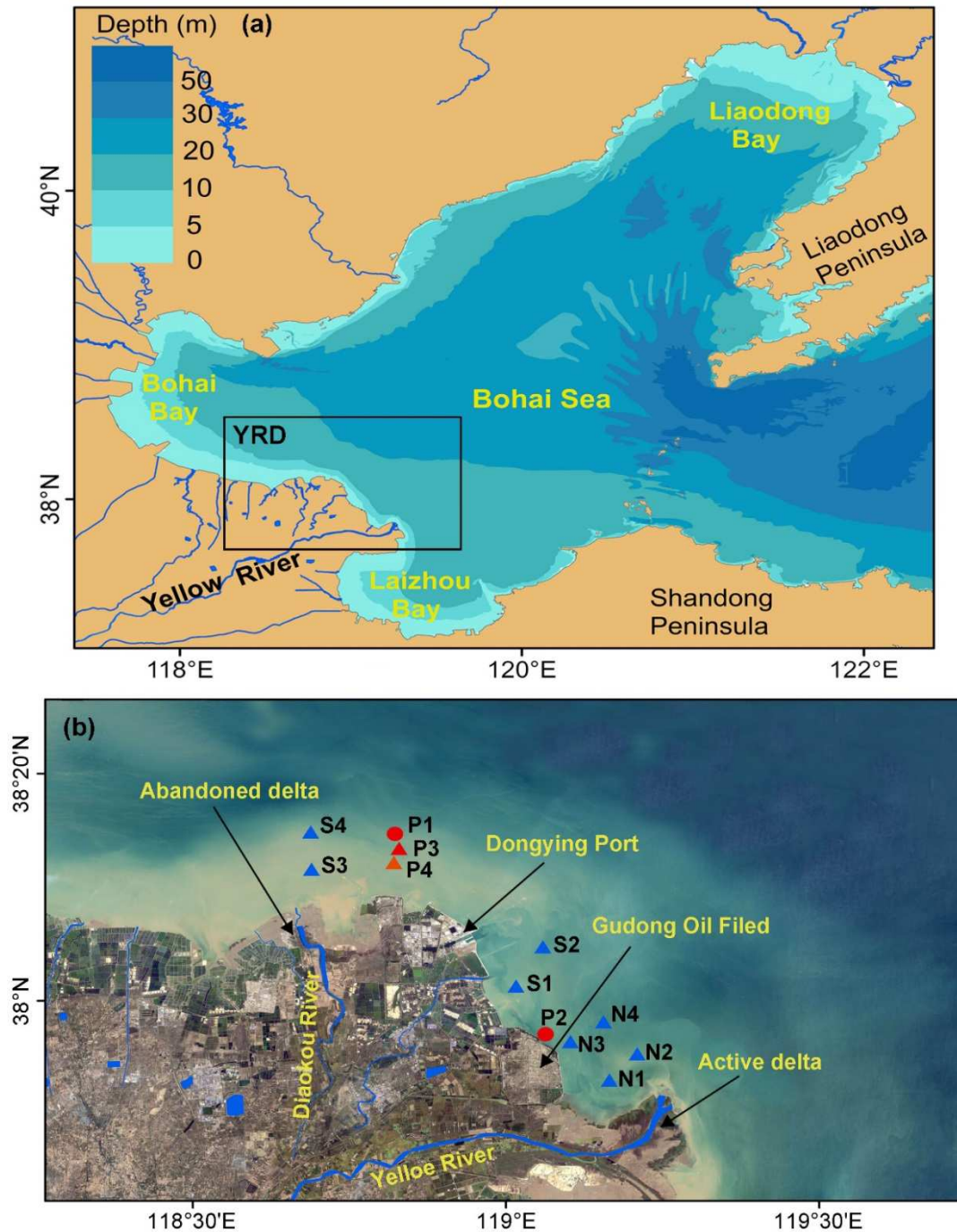
63 As we known, hydrodynamic changes and sediment transport control  
64 morphological evolution of deltas (Gong et al., 2014; Wu et al., 2015). These control  
65 impacts varied at different time scales. Wherein, hydrodynamic changes and sediment

66 transport in storm event can belong to a short-term effect (Ralston et al., 2013;  
67 Anthony, 2015; Florin et al., 2017). However, it is difficult to observe them during the  
68 storm event. Therefore, the numerical model, which integrate hydrodynamics, wave  
69 propagation, sediment transport and morphological changes numerical model, has  
70 provided new indispensable tools to examine the effects of storm events. Numerous  
71 numerical models have been developed with enhanced capability of simulating the  
72 processes of currents, waves, salinities and sediments in delta areas, such as ECOM-si,  
73 and FVCOM for estuarine circulations; ECOMSED for sediment transport; SWAN for  
74 nearshore wave climates; and many other modelling systems, such as ROMS, MIKE 3  
75 (DHI Water and Environment), and Delft3D for regional hydrodynamics and  
76 morphodynamics.

77 The YRD has been gradually formed in the western Bohai Sea (Fig. 1a), since  
78 the Yellow River migrated its main watercourse from the Yellow Sea to the Bohai Sea  
79 in 1855. With the subsequent frequent avulsions both natural and engineered, the  
80 YRD has developed several delta lobes (Fig. 1b), and the significant morphological  
81 evolution of the abandoned delta lobes have been observed in recent decades. For  
82 example, the coastline along the northern YRD and Gudong Oil Field have suffered  
83 serious erosion in recent years (Qi and Liu 2017). Moreover, the energetic winds and  
84 waves generated by storm events have been found to significantly impact on this  
85 coastal region. During storm events, the wave action is particularly prominent off the  
86 YRD, becoming a key factor in controlling sediment resuspension (Jia et al., 2012;  
87 Zhang et al., 2018). Many studies have addressed its shoreline dynamics (Zhang, 2011;



88 Kuenzer et al., 2014; Fan et al., 2018), morphological changes (Kong et al., 2015; Xu  
 89 et al., 2016; Jiang et al., 2017; Wu et al., 2017) and sediment dispersals (Wang et al.,  
 90 2010; Bi et al., 2014; Wu et al., 2015).



91  
 92 **Fig. 1.** (a) Computational domain and topography of the Bohai Sea; (b) Detailed study area, where  
 93 blue triangles mark the locations of the vertical hydrological and sediment measurements and  
 94 other marks represent the locations of continuous survey during the storm event in April 2013.  
 95 Two alongshore sections are also indicated for detailed comparisons.

96           However, little research has been focused on the storm-induced hydrodynamic  
97 and morphological processes, especially in relation to the mechanism of coastal  
98 erosion. Therefore, this study focuses on exploring the hydrodynamic and sediment  
99 characteristics in the YRD during storms using the Delft3D model together with the  
100 measured sediment, wave, and tidal data during a storm event in April 2013, in an  
101 attempt to reveal the storm-induced hydrodynamic changes and seabed erosion.

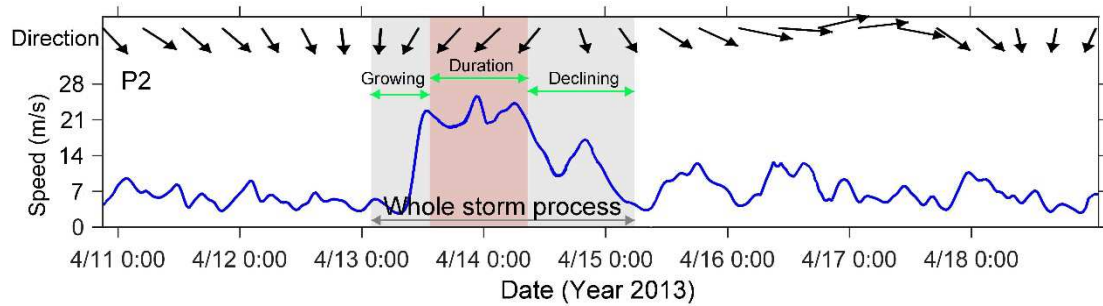
## 102   **2 Model description**

### 103   **2.1 Study area and model grid**

104           The YRD, located in mid-latitude region, is susceptible to storms throughout the  
105 year, especially storms generated by cold-air outbreaks in winter, or in  
106 autumn-to-winter and winter-to-spring seasonal transition (Wu et al., 2002). Such  
107 storms usually lead to intense hydrodynamic changes and significant sea-level  
108 anomalies around the YRD nearshore zone. In 2013, 12 storm surges occurred in the  
109 littoral area of Yellow River Delta, all of which were extratropical storm (Beihai  
110 Branch of State Oceanic Administration People's Republic of China, 2014). Among  
111 them, the storm occurring in April 2013 was selected to simulate based on a coupled  
112 model, which combines hydrodynamic model (Delft3D-FLOW), wave  
113 (Delft3D-WAVE) and sediment transport (Delft3D-SED). In the early stage of this  
114 storm, the northwest wind was dominant. On April 13, 2013, the wind direction  
115 turned to north, and then gradually turned to northeast. The storm event began at 2:00  
116 on April 13 and ended at 3:00 on April 15, and lasted nearly 50 hours from growth to  
117 decline, covering two tidal cycles, in which the wind speed maintained at about 20



118 m/s for 20 hours, from 12:00 on the 13th to 8:00 on the 14th (Fig. 2).

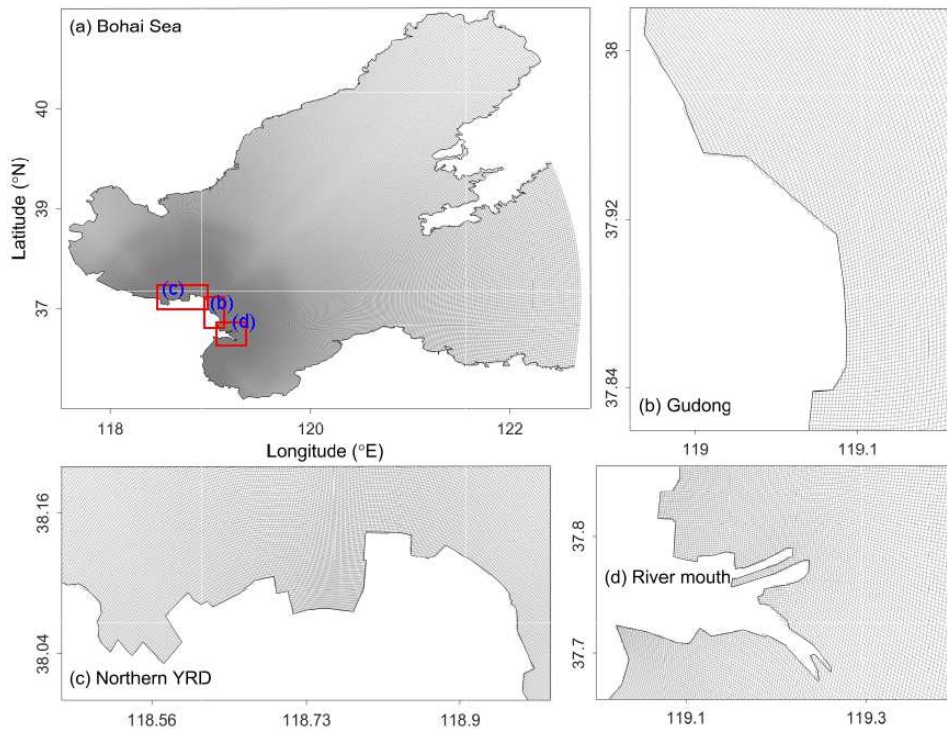


119

120 **Fig. 2.** The wind process during the examined storm.

121 Since the Bohai Sea is a semi-enclosed sea, and cold-air outbreaks mostly occur  
 122 northerly in this region, the model domain was set to cover the entire Bohai Sea, with  
 123 an open boundary in the north Yellow Sea near the Bohai Strait. Curvilinear grid cells  
 124 that cover this domain were generated by Delft3D-RGFGRID with a refined high grid  
 125 resolution used in the areas of interest at the Yellow River subaqueous delta. The total  
 126 number of grid cells was  $771 \times 432$  (Fig. 3 a). The average grid cell spacing was about  
 127 1 km; varying from the maximum mesh size of nearly 2 km at the open boundaries to  
 128 the minimum mesh size of approximately 150 m along the YRD coast (Fig. 3 b-d).  
 129 The topography data were based on the YRD surveys carried out in 2012 for the  
 130 subaqueous delta, with a spatial resolution of 300-500 m, and coastal surveys carried  
 131 out in 2009 for the other part of the Bohai Sea, with a spatial resolution of 1000-5000  
 132 m, respectively (Fig. 3 a). In winter, due to the prevalence of strong northerly wind  
 133 and concomitant high waves (Bi et al., 2011), the distribution of salinity, temperature  
 134 and sediment in the littoral area of YRD is found to be vertically homogeneous,  
 135 indicating a well-mixed water column (Yang et al., 2011). Thus, the model adopted  
 136 seven layers in the vertical direction, and from the bottom layer to surface layer, the

137 values of  $\sigma$  were set to 0.1, 0.1, 0.2, 0.2, 0.2, 0.1, and 0.1.



138

139 **Fig. 3.** (a) Numerical model mesh with the details of: (b) the Gudong coast (c) the northern YRD,  
 140 and (d) the active river mouth. The three red boxes in (a) from top to bottom mark the northern  
 141 YRD, the Gudong coast and the active river mouth, respectively.

## 142 2.2 Initial and boundary conditions

143 Using the modelling system above described, simulations started initially with a  
 144 static state from the mean sea level, and zero flow velocity and sediment  
 145 concentration in the domain. The coastline boundaries were determined from the  
 146 high-water lines with a spatial resolution of 15 m, which were extracted from the false  
 147 color composite images of Landsat OLI data. The model was driven by the tide  
 148 forcing along the open boundary, consisting of 8 main tidal constituents, i.e. M2, S2,  
 149 N2, K2, K1, O1, P1 and Q1, as well as surface forcing from the ECMWF (European  
 150 Centre for Medium-Range Weather Forecasts) wind and atmospheric pressure data  
 151 with a spatial resolution of  $0.25^\circ \times 0.25^\circ$  (latitude  $\times$  longitude). Compared with the

152 storm scale in the Bohai Sea, this resolution is sufficient for modeling land-ocean  
153 gradients (Lv et al, 2014).

154 Suspended sediment concentration (SSC) at seaward boundary was set to 0, since  
155 the open boundary is far from the interested area and the water depth is mostly deeper  
156 than 30 m, so that the impact of sediment conditions from the open boundary on the  
157 sediment transport in the nearshore region which was based on the local equilibrium  
158 transport formula can be neglected. At landward boundary, distinct seasonal variation  
159 of sediment delivery occurs from the Yellow River. River discharge boundary  
160 conditions were imposed appropriately based on daily-averaged water discharge and  
161 sediment concentration recorded from the Lijin hydrological station, provided by the  
162 Yellow River Water Resource Commission.

### 163 **2.3 Parameter settings**

164 The bottom friction was parameterized using the Manning coefficient  $n$ ,  
165 calculated from the water depth (Xing et al., 2012):

$$n=(0.015 + 0.01/h) , h>1 \quad (1)$$

166 where  $h$  is the water depth (m). The bottom roughness for regions water depth below  
167 1 m is prescribed by a uniform Manning coefficient of 0.025, which is the result of  
168 verification of the coupled model. It should be noted that the Manning coefficient was  
169 defined differently in Delft3D as  $M_n=1/n$ . The horizontal eddy viscosity and  
170 diffusivity are calculated with the Horizontal Large Eddy Simulation (HLES) sub-grid  
171 model.

172 According to Ren et al. (2012), the seabed composition off the YRD is highly

173 variable in space, and the median grain size ( $D_{50}$ ) varies widely from  $\sim 5$  to  $\sim 133$   $\mu\text{m}$ .  
 174 Therefore, multiple sediment fractions were considered in the morphological model.  
 175 In this study, four mud fractions (fine to coarse, denoted as md1–md4) were used to  
 176 represent nearly the full range of cohesive sediment grain sizes (4, 7.5, 28, and 62.5  
 177  $\mu\text{m}$ ). Specifically, one sand fraction (100  $\mu\text{m}$ ) was included in the model, i.e., the  
 178 dominant fine sand fraction (denoted as sd1), to reduce the overestimation of erosion  
 179 along the coasts. The settling velocity ( $w_s$ ) of each mud fraction was determined  
 180 relative to the grain size after calibrating the model against the spatial distribution of  
 181 depth-averaged SSC.

182 Critical erosion shear stress  $\tau_{ce}$  was a key parameter for simulating fine-grained  
 183 sediment transport. For the critical shear stress of the cohesive sediment, the  
 184 following formulas were used (Dou, 1999; Lu et al., 2011):

$$\tau_{ce} = k^2 \rho \left( \frac{d'}{d^*} \right)^{\frac{1}{3}} \left[ 3.6 \frac{\rho_s - \rho}{\rho} g D_{50} + \left( \frac{\gamma_0}{\gamma_0^*} \right)^{\frac{5}{2}} \left( \frac{\varepsilon_0 + gh\delta\sqrt{\delta/D_{50}}}{D_{50}} \right) \right] \quad (2)$$

185 where  $\rho_s$  is the specific sediment density, 2650  $\text{kg m}^{-3}$ ;  $\rho$  is the fresh water density,  
 186 1000  $\text{kg m}^{-3}$ ;  $g$  is gravity acceleration, and  $D_{50}$  is median size of sediment;  $\varepsilon_0$  is  
 187 comprehensive cohesion coefficient, 1.75  $\text{cm}^3/\text{s}^2$ ;  $k$  is a coefficient of different status  
 188 of incipient motion, 0.128;  $\delta$  is the thickness of pellicular water, and  $\delta = 2.31 \times 10^{-5}$   
 189 cm. In this study,  $d' = 0.5$  mm when  $D_{50} < 0.5$  mm, and  $d^* = 10$  mm accordingly.  
 190 Initial dry bulk density  $\gamma_0$  is:

$$\gamma_0 = \rho_s (1 - e_0 \eta) \quad (3)$$

191 and steady dry bulk density  $\gamma_0^*$  is:

$$\gamma_0^* = \rho_s \left(1 - \frac{\pi}{6} (1 - 2\sqrt[3]{D_{50}})\right) \quad (4)$$

192 where  $e_0$  is the maximum porosity, and we used  $e_0 = 0.625$ . For all the mud  
 193 fractions, the erosion parameter  $M$  is  $5.0 \times 10^{-5}$  kg/m<sup>2</sup>/s, the specific density is 2650  
 194 kg/m<sup>3</sup>, and the dry bed density is 500 kg/m<sup>3</sup>.

195 The erosion and deposition fluxes for cohesive sediment (< 64 μm) were  
 196 calculated applying the following Partheniades-Krone formulations:

$$E_i = M_i \left( \frac{\tau_b}{\tau_{b,i}} - 1 \right), \text{ when } \tau_{cw} > \tau_{cw,i}, \text{ else } E_i = 0 \quad (5)$$

$$D_i = w_{s,i} c_{b,i} \quad (6)$$

197 where  $E_i$ ,  $D_i$  and  $M_i$  are the erosion flux, deposition flux and erosion parameter of  
 198 the  $i$ th mud fraction (kg/m<sup>2</sup>/s), respectively;  $w_{s,i}$  is the settling velocity of the  $i$ th mud  
 199 fraction (m/s);  $c_{b,i}$  is the depth-averaged concentration of the  $i$ th mud fraction  
 200 (kg/m<sup>3</sup>);  $\tau_b$  is the combined bed shear stress due to currents and waves (N/m); and  
 201  $\tau_{b,i}$  is the critical shear stress for erosion of the  $i$ th mud fraction (N/m<sup>2</sup>). For 2D  
 202 depth-averaged flow bed shear stress induced by a turbulent flow is assumed to be  
 203 given by a quadratic friction law:

$$204 \quad \tau_b = \frac{\rho_0 g \bar{U} |\bar{U}|}{C_{2D}^2} \quad (7)$$

205 Where  $\bar{U}$  is the magnitude of the depth-averaged horizontal velocity. Due to finest  
 206 fractions can be entrained into the seabed (Winterwerp et al., 2007), the critical shear  
 207 stress for deposition was omitted in the model, which means that continuous  
 208 deposition was specified in the model. All those parameters used in the mode  
 209 simulations are summarized in Table 1.

210 **Table 1**

211 Sediment and mud fractions considered in the morphological model

Type	Fraction	$D_{50}$ ( $\mu\text{m}$ )	$\tau_{ce}$ ( $\text{N/m}^2$ )	$w_s$ (mm/s)	$M$ ( $\text{kg/m}^2/\text{s}$ )
Mud	md1	4	Spatially varying	0.06	$5.0 \times 10^{-5}$
	md2	7.5		0.14	
	md3	28		0.22	
	md4	62.5		0.26	
Sand	sd1	100	–	–	–

212 The sediment transport processes responsible for bed-level changes vary greatly  
 213 off the YRD due to the spatial variations of the bed sediment grain size. Therefore,  
 214 our model considers both non-cohesive (sand) and cohesive sediment (mud), which  
 215 are treated separately in Delft3D, and sand-mud interactions are excluded as a first  
 216 approximation. Suspended sediment transport is calculated by solving the  
 217 depth-averaged advection-diffusion equation, which includes source and sink terms  
 218 and is presented below:

$$\frac{\partial hc_i}{\partial t} + \frac{\partial huc_i}{\partial x} + \frac{\partial hvc_i}{\partial y} = \frac{\partial}{\partial x} (h\varepsilon_h \frac{\partial c_i}{\partial x}) + \frac{\partial}{\partial y} (h\varepsilon_h \frac{\partial c_i}{\partial y}) + S_i \quad (7)$$

219 where  $c_i$  is the sediment concentration of the  $i$ th sediment fraction ( $\text{kg/m}^3$ ),  $u$  and  $v$   
 220 are horizontal velocity components (m/s),  $\varepsilon_h$  is horizontal eddy diffusivity ( $\text{m}^2/\text{s}$ ),  
 221 and  $S_i$  is the source and sink term of the  $i$ th sediment fraction representing the  
 222 exchange between the water column and the bed. For non-cohesive sediment transport  
 223 ( $\geq 64 \mu\text{m}$ ), we follow the approach of Van Rijn (1993).

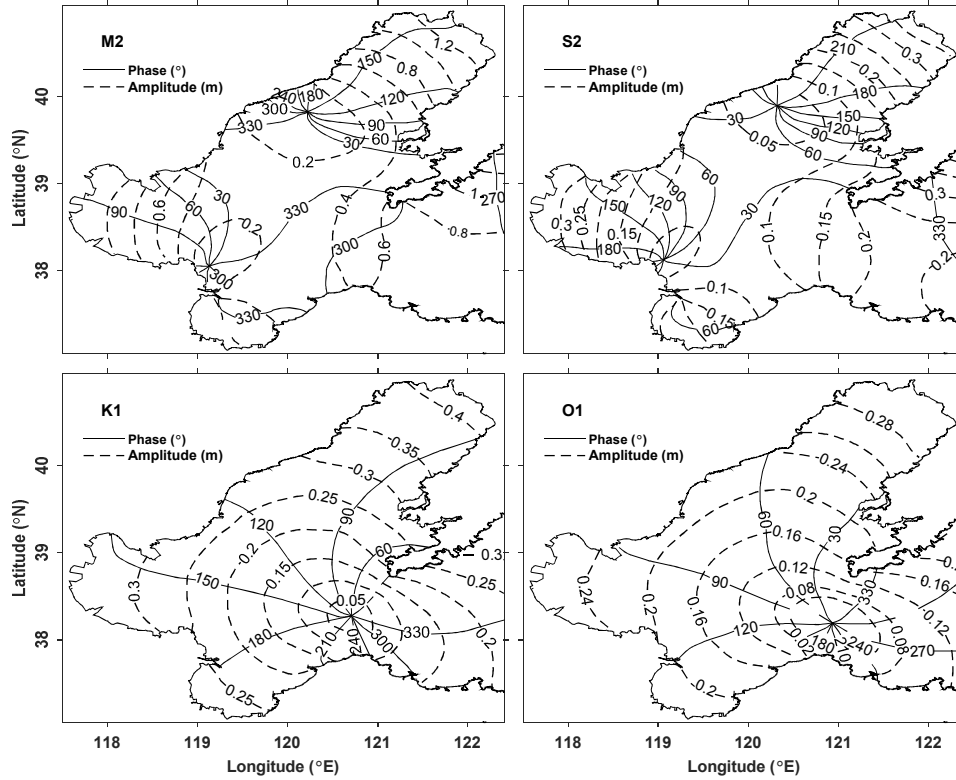
## 224 **3 Model validations**

### 225 **3.1 Tidal regime**

226 The tides in the Bohai Sea are relatively small and fall into the  
 227 micro-tidal/mixed-semidiurnal categories. Tides from the northwest Pacific



228 propagates into the Bohai Sea through the Bohai Strait. There are two amphidromic  
229 points for semidiurnal tidal constituents (M2 and S2) in the Bohai Sea: one at the  
230 offshore area of Qinhuangdao and the other near the Yellow River mouth. One  
231 amphidromic point for diurnal tidal constituents (K1 and O1) appears in the Bohai  
232 Strait. The tidal model ran 30 days in order to obtain tidal constituents harmonic  
233 constants. Harmonic constants of tidal elevation of each constituent are obtained by  
234 applying harmonic analysis to modeled time series of sea level at each model grid.  
235 The results showed that our model successfully simulated tide systems. The co-tidal  
236 and co-range lines for M2, S2, K1, O1 constituents (Fig. 4) fitted well with  
237 observations (Chen et al., 1992) and the results of Huang (1995). The changes of the  
238 YRD influenced its surrounding tidal wave and obstructed tidal energy (Pelling et al.,  
239 2013), and the amphidromic points here calculated using new coastlines were farther  
240 to land than previous studies. Also, this result agreed well with other publications  
241 (Hao et al., 2010).



242  
 243 **Fig. 4.** Co-tidal charts of M2, S2, K1, O1 constituents from the model simulations (dotted and  
 244 solid lines indicating the amplitude and phase, respectively).

### 245 3.2 Tide velocity

246 The accurate prediction of flow velocity and direction was a crucial step for the  
 247 simulations of sediment transport which strongly depends on the shear stress,  
 248 deposition criterion, and turbulence characteristics in the bottom boundary layer. The  
 249 time series of currents and SSCs measured along the YRD coast were used to validate  
 250 the model in normal conditions. The observations were taken at eight sites, as shown  
 251 in Fig. 1b, at N1, N2, N3 and N4 in July 2009, and S1, S2, S3 and S4 in October 2009.  
 252 The correlation coefficient (CC), the skill score (SS), and the root mean square errors  
 253 (RMSE) were calculated to evaluate the quality of the model performance:

$$CC = \frac{\sum (X_{mod} - \bar{X}_{mod})(X_{obs} - \bar{X}_{obs})}{[\sum (X_{mod} - \bar{X}_{mod})^2 \sum (X_{obs} - \bar{X}_{obs})^2]^{1/2}} \quad (8)$$

$$SS = 1 - \frac{\sum (X_{mod} - X_{obs})^2}{\sum (X_{mod} - \bar{X}_{obs})^2} \quad (9)$$

$$RMSE = \sqrt{\frac{\sum (X_{mod} - X_{obs})^2}{N}} \quad (10)$$

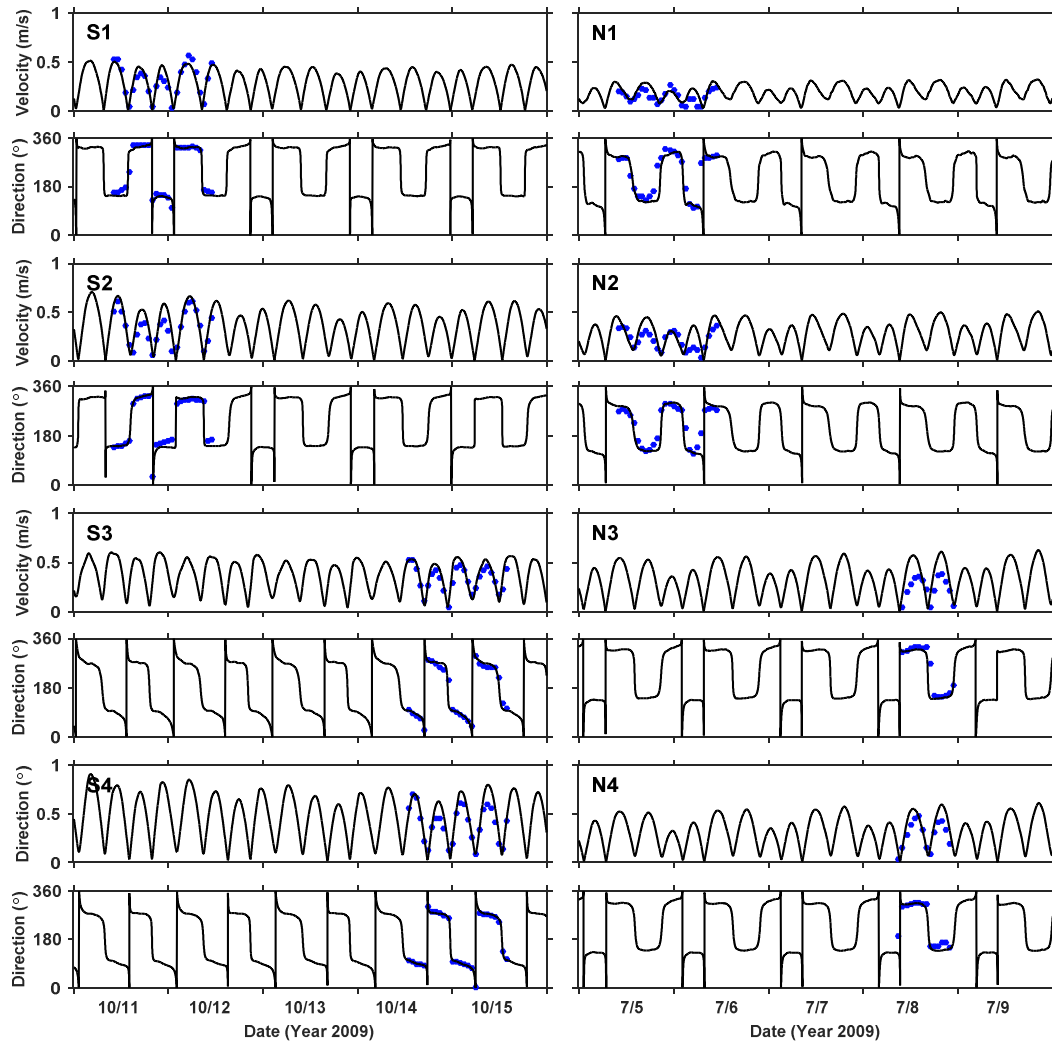
254 where  $X_{mod}$  is the modeled result and  $X_{obs}$  is the observed data. The performance of  
 255 model is classified as suggested by Allen et al., 2007; Ralston et al., 2010; Luo et al.,  
 256 2017 as show in Table 2.

257 **Table 2**

258 Classification of model performance

SS	>0.65	0.65-0.5	0.5-0.2	<0.2
Performance	Excellent	Very good	Good	Poor

259 We first validated the simulations with the normal conditions. The model  
 260 simulation began June 15, 2009. After running for half a year with the observed runoff  
 261 and 6-hourly ECMWF re-analyzed wind, the model results were output for  
 262 comparison. Comparisons of the depth-averaged flow velocity and direction with the  
 263 model results and the observation data are shown in Fig. 5. The type of tidal current  
 264 was semidiurnal and rectilinear, and the velocity curve showed four peaks and four  
 265 valleys within one day. Statistical assessments of validation are shown in Table 3. It is  
 266 clear that the average  $CC$  of flow velocity at N1-N4 was 0.78, which was lower than  
 267 those at S1-S4, 0.89, because those sites locate at the river mouth, the estuarine  
 268 circulation is rather complicated. The average  $SS$  at S1-S4 and N1-N4 was 0.62 and  
 269 0.49 (Table 3), respectively, ranking “very good” and “good” according to the  
 270 categories described above. The  $RMSE$  were also reasonable.



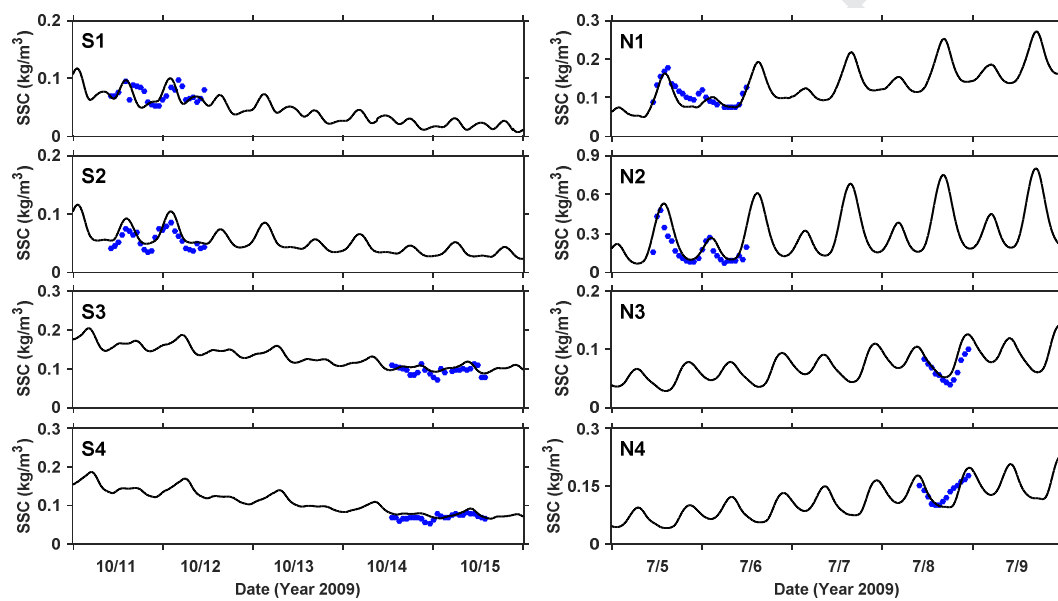
271

272 **Fig. 5.** Comparison of measured depth-average flow velocity and flow direction (blue dots) with  
 273 the computed results (solid line) at eight measurement locations.

### 274 3.3 Suspended sediment concentration

275 The computed SSCs were compared with the observed SSCs at Sites S1-S4 and  
 276 N1-N4 (Fig. 6). The computed SSC was well reproduced with tidal variation. For  
 277 example, the tide had a transition from spring tides to neap tide during Oct 11 to Oct  
 278 15, 2009, so the modeled SSCs of sites S1-S4 during the period had decrease trends.  
 279 The modeled SSC had the same order of magnitude as the measurements. The  
 280 relatively large errors between the modeled and observed data appearing at sites S3  
 281 and S4 were mainly due to the erosion caused by waves, which was difficult to

282 estimate during neap tides. The average *SS* of SSC at sites S1-S4 and N1-N2 (not with  
 283 N3 and N4 because of less samples) were 0.24 and 0.26 (Table 3), indicating that the  
 284 model performed satisfactory. The *CC* and *RMSE* in Table 2 also illustrated the good  
 285 performance of the model. The results clearly indicate that the model was properly set  
 286 up and can be used to study the dynamics of sediment process off the YRD coast  
 287 during normal conditions.



288  
 289 **Fig. 6.** Comparison of depth-average flow velocity and flow direction between the simulated  
 290 (solid line) and the observed (blue dots) at eight sites.

291 **Table 3**

292 Correlation Coefficient, Root-Mean-Square Error, and Skill Score of each measured site

	S1-S4 (average)			N1-N4 (average)		
	CC	SS	RMSE	CC	SS	RMSE
Velocity (m/s)	0.89	0.62	0.08	0.78	0.49	0.11
SSC ( $\text{kg}/\text{m}^3$ )	0.57	0.24	0.05	0.62	0.26	0.04

### 293 3.4 Storm validations

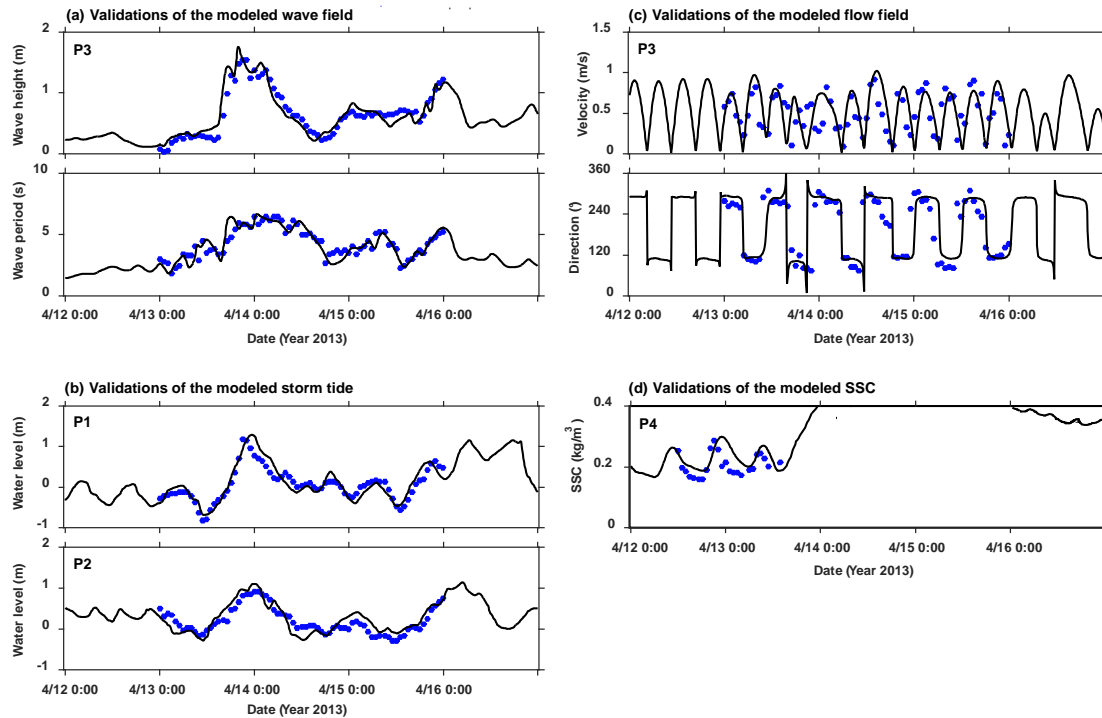
294 The measured data during a storm in April 2013 were employed for storm  
 295 verification of hydrodynamic and sediment characteristics. More details of this survey  
 296 can be seen in the work by Quan (2014) and Bian et al (2016). The water levels data

297 were provided by Central Platform of Shengli Oil Field (P1, locations are labeled in  
298 Fig. 1b) and Gudong gauge station (P2). The flow and wave data were collected with  
299 an ADCP (Acoustic Doppler Current Profilers) at P3, and the SSC data were collected  
300 with a turbidity meter (OBS-3D) at P4.

301 To verify the accuracy of the coupled Delft3D-WAVE model, the P3 site was  
302 selected to compare the wave height and period between observation and simulation  
303 during the storm period of April 15-17 2013 (Fig. 7). The SWAN model generally  
304 well-reproduced variations of the significant wave height and period (Fig. 7a). A cold  
305 front passed on the April 13, resulting in a marked increase in wave height (maximum  
306 wave height of approximately 2.0 m). The simulated wave heights were slightly  
307 underestimated due to the low temporal resolution of the meteorological forcing,  
308 which was unable to capture the peaks of wind velocities values adequately. The skill  
309 assessments are summarized in Table 4. The *SS* of wave height was 0.41, ranking  
310 “good” according to the categories described above. The *CC* and *RMSE* were also  
311 reasonable. Through comparison between simulated and observed storm tide at P1  
312 and P2 sites (Fig. 7b), the maximum and minimum water level as well as the phase  
313 were in reasonable agreement with the measurements. The *SS* of storm tide at site P1  
314 and P2 was 0.26 and 0.27, respectively, which indicated the reasonableness of storm  
315 tide verification. The flow and SSC validations are shown in Fig. 7c and Fig. 7d. The  
316 model reproduced a similar sectional pattern to the survey, specifically, the *SS* of flow  
317 velocity and SSC were 0.51 and 0.21, and the *CC* were 0.65 and 0.49, respectively.  
318 Verification results showed that model predictions during storm period based on the



319 model were quite consistent with the observations at these sites.



320

321 **Fig. 7.** Comparison of depth-average flow velocity and direction between the simulated (solid line)  
 322 and the observed (blue dots) at eight sites.

323 **Table 4**

324 Correlation Coefficient, Root-Mean-Square Error, and Skill Score of each measured site

	P1, P2 (average)			P3			P4		
	CC	SS	RMSE	CC	SS	RMSE	CC	SS	RMSE
Wave height (m)	-	-	-	0.84	0.71	0.13	-	-	-
Storm surge (m)	0.89	0.73	0.18	-	-	-	-	-	-
Velocity (m/s)	-	-	-	0.65	0.51	0.11	-	-	-
SSC ( $\text{kg}/\text{m}^3$ )	-	-	-	-	-	-	0.49	0.21	0.06

## 325 4 Results and discussion

326 In total, three runs were considered in this study to examine the impacts of storm  
 327 conditions on hydrodynamics and sediment transport over the nearshore seabed of  
 328 YRD, as shown in Table 5. Run 1 (control run) was embedded into a  
 329 wave-tide-circulation coupled model and driven by climatological daily mean river  
 330 discharge and calm wind (speed below 3 m/s) as well as water flux and salinity in  
 331 open ocean boundary. We can understand the characteristics of hydrodynamics and

332 sediment in normal conditions from the control run. In Run 2, the calm wind and  
 333 normal atmospheric pressure conditions used in Run 1 were replaced by strong wind  
 334 and low atmospheric pressure conditions (data from ECMWF) for setting storm  
 335 conditions. By comparing the results of these two runs, we can quantitatively identify  
 336 storm impacts. In addition, Run 3 was conducted with storm conditions without tides.  
 337 The impacts of storm-induced wave on the seabed erosion were examined by  
 338 comparing the results of three runs.. All the numerical experiments were run over a  
 339 period of one month, beginning on April 1, 2013, and the data calculated by the model  
 340 from April 13 to April 15 were used to analyze the hydrodynamic processes and  
 341 sediment transport.

342 **Table 5**

343 Three different conditions for model simulations

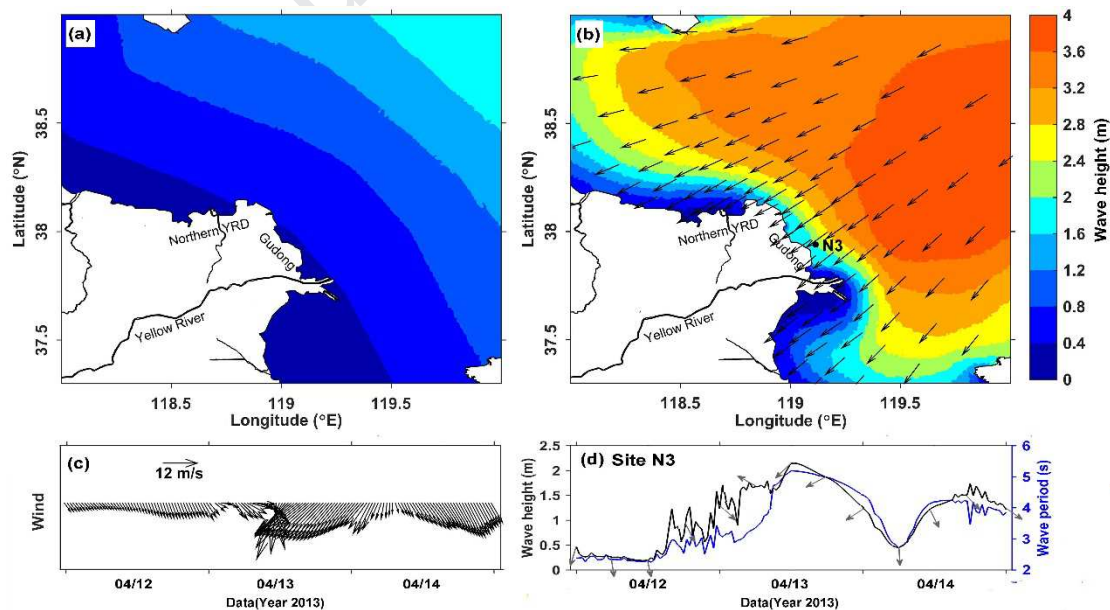
Simulation	Tide	Wind	Waves
Run 1 (control run)	Yes	No (normal condition)	Yes
Run 2	Yes	Strong	Yes
Run 3	No	Strong	Yes

#### 344 **4.1 Waves**

345 Calm winds forcing for Run 1 typically produced waves with significant wave  
 346 height of less than 0.8 m (Figure 8a), and period of less than 3 s in the study area. The  
 347 weak wave dynamic is attributed to the causes of wave in this area. The Bohai Sea has  
 348 poor water exchange capacity with open ocean due to its narrow strait occupied by  
 349 islands. Surface waves are generated by local winds.

350 The time series of wind stress for Run 2 are shown in Fig. 8c from April 12 to 14,  
 351 2013. The wind vectors were surface area averaged off the YRD, and on the  
 352 conventional geographical coordinate system. As shown in the Fig. 8c, strong wind

353 (more than 12 m/s) began in the morning of April 13 with directions moved from  
 354 northwest to the northeast on April 13 and moved the northwest again on April 14.  
 355 The northeasterly wind speeds shown two acceleration processes, in the morning and  
 356 the end of April 13, respectively. The results from Run 2 showed that the wave height  
 357 of approximately 2 m along the Gudong coast under the maximum wind speed, and  
 358 the wave height of more than 1.2 m along the northern YRD coast (Fig. 8b). The time  
 359 series of significant wave height, direction and period of site N3 is presented in Fig.  
 360 8d to show the changes at temporal scales of wave features. It can be seen that the  
 361 significant wave height and period were generally accordant with wind speed, and the  
 362 wave directions changed with wind directions. The significant wave height reached its  
 363 maximum, more than 2 m, at site N3, during the first wind acceleration process of  
 364 northeasterly wind, and reached more than 1.5 m during the second wind acceleration  
 365 process.



366  
 367 **Fig. 8.** (a) Significant wave height during calm condition forcing for Run 1. (b-d) Wave features  
 368 during the examined storm: (b) significant wave height and direction with the maximum wind  
 369 speed; (c) time series of surface area averaged wind vector off the YRD (118-120°E, 37.3-38°N);

370 (d) significant wave height (black line), direction (gray arrow) and period (blue line) at site N3.

## 371 **4.2 Currents**

### 372 *4.2.1 Water mass transport*

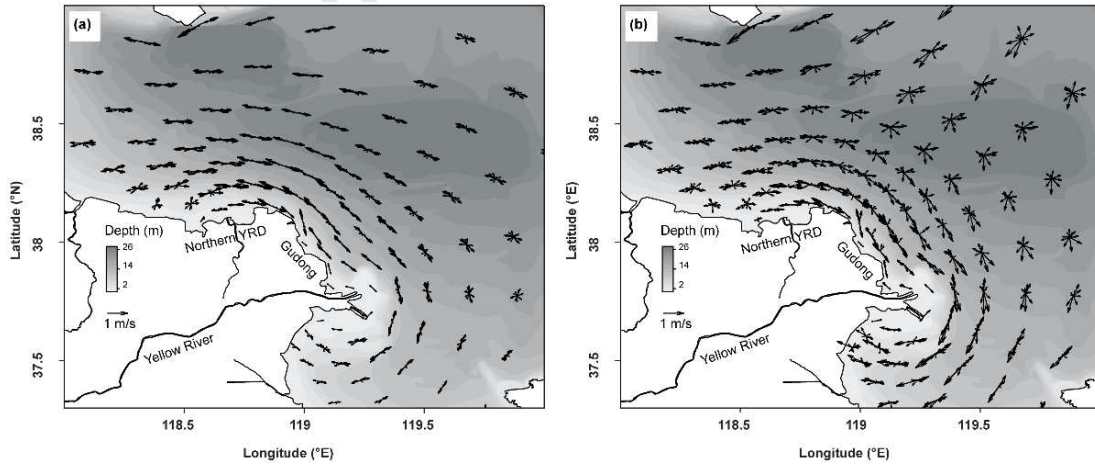
373 Storm-induced seaward coastal sediment transport can be key for to the inner  
374 shelf (Goff et al., 2010). To investigate the impacts of storm-surge flood and ebb on  
375 sediment transport, we first examined storm-induced current fields. The model runs  
376 were either forced by calm wind (Run 1), or strong northerly wind (Run 2). Fig. 9a  
377 shows the current was reciprocated with southeastern flood and northwestern ebb in  
378 normal conditions, with areas of high current velocity locating off the northern YRD  
379 coast and the active river mouth. Reciprocated current was predominant in shallow  
380 area (roughly within the 15m isobaths), while it gradually turned into rotated current  
381 with the increase of water depth. In storm conditions, not only the current velocities  
382 increased, especially the flood velocity, but the directions were also changed: rotated  
383 current was predominant (Fig. 9b). Special attention should be paid to the feathers in  
384 the shallow area: most of these current vectors were along the flood-ebb axis or  
385 directed to the right side of the ebb direction. Nonlinear interaction between the tide,  
386 wind-driven current, and the Coriolis force should be responsible for this phenomenon.  
387 Huang et al. (1996) and Cao and Lou (2011) suggested that on the surface, the  
388 wind-driven current flows along the wind direction. During flood tide, wind-driven  
389 current added to tide current, the water mass could flow to southeast with higher  
390 velocity. During ebb, when the sea surface elevation decreases, the tidal water  
391 returned to the outlets hard and flowed north-northwestward, opposing with  
392 wind-driven current, and the water mass could turn into right-neighbored outlets.

393 Wind intensity and direction can generate changes in residual currents in the shallow  
 394 areas, which are also found in the shore of the Tagus Estuary (Vaz and Dias, 2014).

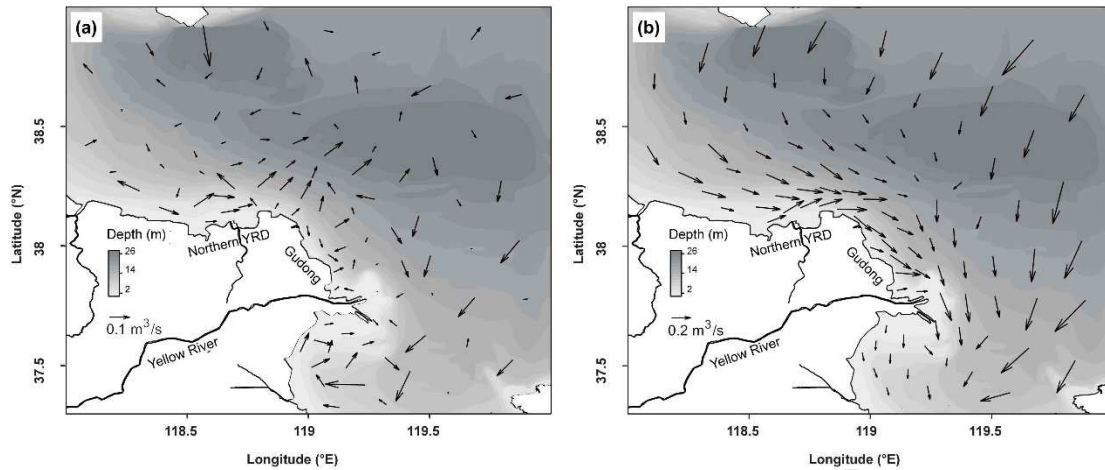
395 In order to quantitatively reveal the contributions of the storm to water mass  
 396 transport, the residual transport of water ( $Tr_w$ ) through a unit width was calculated,  
 397 which can be defined as follows:

$$Tr_w = \frac{1}{T} \int_0^T \int_{-H}^{\eta} \vec{V}(x, y, z, t) dt \quad (11)$$

398 where  $\eta$  is the surface elevation,  $H$  is the still water depth, and  $\vec{V}$  is the horizontal  
 399 velocity vector, and  $T$  is the time period. Previous studies (Wu et al., 2014, 2018)  
 400 showed that residual transport velocity is a more reasonable method than the Eulerian  
 401 residual current to index the subtidal transport in the shallow coastal water. In this  
 402 study, 3 d (from 0:00 on April 13 to 16 April), were used as an statistical time window  
 403 to obtain the  $Tr_w$  in normal and storm conditions, respectively, as shown in Fig. 10.



404  
 405 **Fig. 9.** Tide velocity vectors of depth-averaged current during an ebb-flood process in (a) normal  
 406 conditions and (b) storm conditions.



407

408 **Fig. 10.** Residual water mass transport in (a) normal and (b) storm conditions.

409 In normal conditions, the influence of wind was weak, and the residual currents  
 410 were greatly affected by tidal current. In the shallow area, the  $Tr_w$  was generally less  
 411 than  $0.1 \text{ m}^3/\text{s}$ . Affected by the northerly strong wind, the residual transport of water  
 412 was transported southward in storm conditions, and the  $Tr_w$  was generally greater  
 413 than  $0.2 \text{ m}^3/\text{s}$ , which was 2 to 4 times as large as that in normal conditions. Deep  
 414 water mass transports southwest as a whole, while it begins to transports southeast  
 415 gradually after reaching the central part of the Bohai Bay. Off the northern YRD, the  
 416 residual currents flow eastward along the E-W coast. The direction of residual current  
 417 along the Gudong coast was southeast in storm conditions, basically consistent with it  
 418 in normal conditions. While, converging the water masses from the shallow area of  
 419 the Bohai Bay and the northern YRD, and supported by the water mass from deep  
 420 area, water mass in this area performs a notable transport rate, which was 4 times  
 421 larger than it in normal conditions. The water transport rate off the river mouth also  
 422 significantly increase, and massive water was transported to the central area of the  
 423 Laizhou Bay with the northward inflow. This water transport model also explains why  
 424 high water level always occurs in the Laizhou Bay and the Bohai Bay during storms



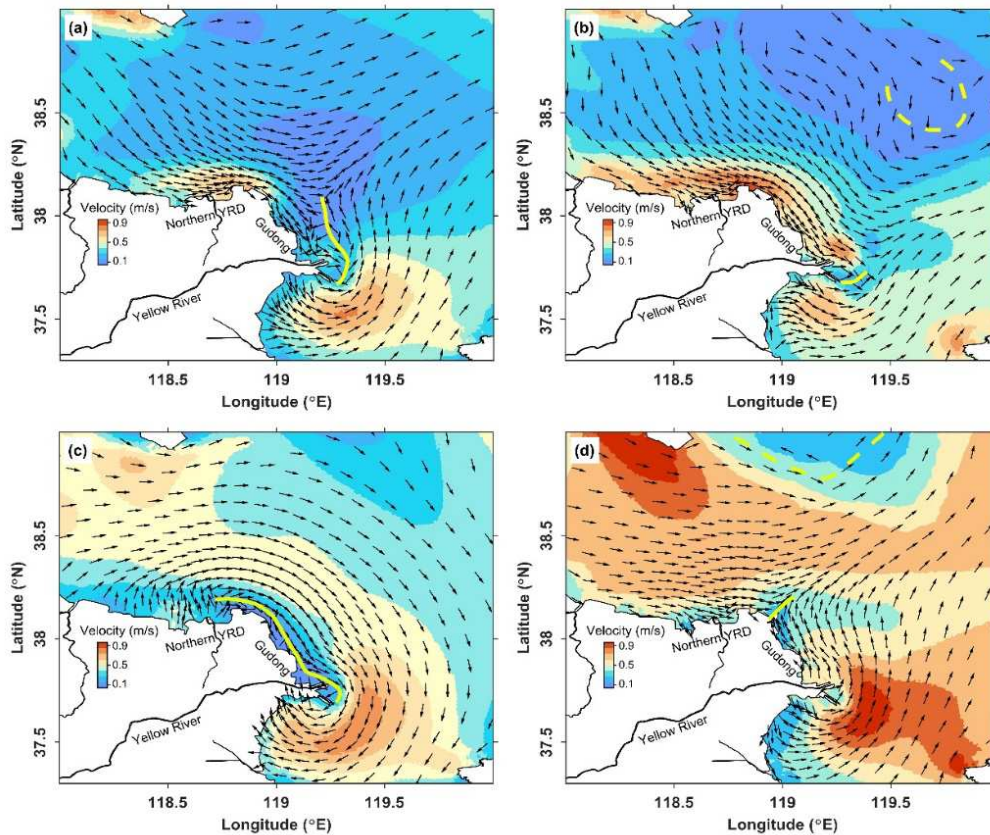
425 (Li et al., 2016).

#### 426 *4.2.2 Tidal shear front*

427 Tidal shear front is an interface between two water bodies with opposing flow  
428 directions and significant low velocity zone, which are instantaneous extraordinary  
429 gradients closely related to sediment dynamics and morphological variabilities (Wang  
430 et al., 2007). Tidal shear front in the littoral area of the YRD has been observed and  
431 modeled in the previous studies (Qiao et al., 2008; Wang et al., 2017). The front was  
432 first reported by Li et al. (1994) who concluded that the shear front, occurring twice  
433 during a tidal cycle, could be classified into two types: inner-flood-outer-ebb (IFOE)  
434 and inner-ebb-outer-flood (IEOF).

435 From Run 1, both types of tidal shear front were observed in normal conditions,  
436 and shown in Fig. 11a and Fig. 11c, respectively. The IEOF type was closer to land  
437 and grows to the northern YRD with larger range than the IFOE type. While, strong  
438 winds had a predominant impact on tidal shear front. Under the pressure of northerly  
439 wind, both the IFOE type (Fig. 11b) and the IEOF type (Fig. 11d) have been  
440 weakened with smaller ranges of tidal shear front than in the normal conditions.  
441 Besides, the trends of tidal shear front changed to be perpendicular to the coasts  
442 comparing with the parallel trends in normal conditions, and the low velocity zones  
443 along the YRD coast disappeared, especially at the IFOE type happens (Fig. 11b).  
444 These changes of tidal shear front were because of the formation of rotated currents in  
445 deep area in strong wind circumstance: tides through rotated currents complete phase  
446 changes, not entirely form oppose-direction flow in shallow area. The changes such as

447 weakened shear front, disappearance of low velocity zone, were benefit for the  
 448 sediment resuspension and dispersal.



449  
 450 **Fig. 11.** Locations of tidal shear front of (a) and (b) IFOE type in Runs 1 and 2; and (c) and (d)  
 451 IEOF type in Runs 1 and 2. The yellow solid lines represent the fronts, and the dashed lines  
 452 represent the ranges of rotated currents.

### 453 4.3 Sediment process

#### 454 4.3.1 SSC

455 The suspended sediment off the YRD is either introduced by river sources or  
 456 resuspended from the seabed in response to various forcing conditions. We first  
 457 performed process study to examine suspended sediment distributions. The simulated  
 458 distribution of depth-averaged SSC from Run 1 and Run 2 are shown in Fig. 12a and  
 459 Fig. 12b, respectively. When using Landsat data to create sediment color images, we  
 460 can estimate the simulated results. For example, we chose the Landsat ETM+ data for

461 22 March 2014 (3.6 m/s average wind speed at S1-S4 and N1-N4) and 27 November  
462 2012 (10.2 m/s average wind speed at S1-S4 and N1-N4) to show the turbid water  
463 distribution in normal and storm conditions, respectively. The model reproduced  
464 distribution of SSC matches well with the satellite images in Fig. 13, and compared  
465 well with the observed data (Yang et al., 2011b; Wang et al., 2014) and the satellite  
466 ocean color data (Zhang et al., 2014).

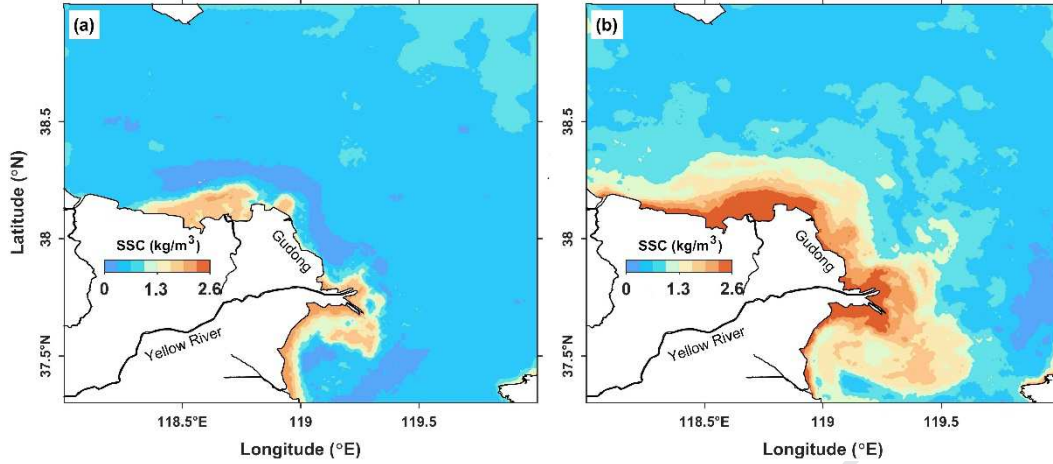
467 Bottom shear stress is an important dynamic factor for sediment erosion and  
468 deposition. When the bottom shear stress is greater than the critical bottom shear  
469 stress, the bottom sediment will be suspended. The total bottom shear stress ( $\tau_{cw}$ ) is  
470 composed of current-induced bottom shear stresses ( $\tau_c$ ) and wave-induced bottom  
471 shear stresses ( $\tau_w$ ) under wave-current interaction. The  $\tau_c$  and  $\tau_{cw}$  could be obtained  
472 from the Run 1 and Run 2, by Formula (7). To further understand the effect of  $\tau_w$  on  
473 the formation of the sediment plume, a numerical Run 3 was conducted in which only  
474 wave and strong wind were included. Fig. 14a, 14b and Fig. 14c show the 3-day  
475 average  $\tau_c$ ,  $\tau_w$  and  $\tau_{cw}$  in the storm conditions, respectively.

476 High SSC values were observed in two regions under normal conditions (Fig.  
477 12a) and formed two substantial sediment plumes, one nearshore the northern YRD  
478 and the other at the active river mouth, with a value about  $1.5 \text{ kg/m}^3$ . The sediment  
479 plume of the river mouth diffuses to the south, which results in the higher SSC in the  
480 northern area of Laizhou Bay. Off the Gudong coast, the SSC was relatively low, less  
481 than  $0.5 \text{ kg/m}^3$ . The distribution of high and low SSC is consistent with that of  $\tau_c$   
482 (Fig. 14a), which indicates that the  $\tau_c$  is strong enough to stir the bottom sediment,

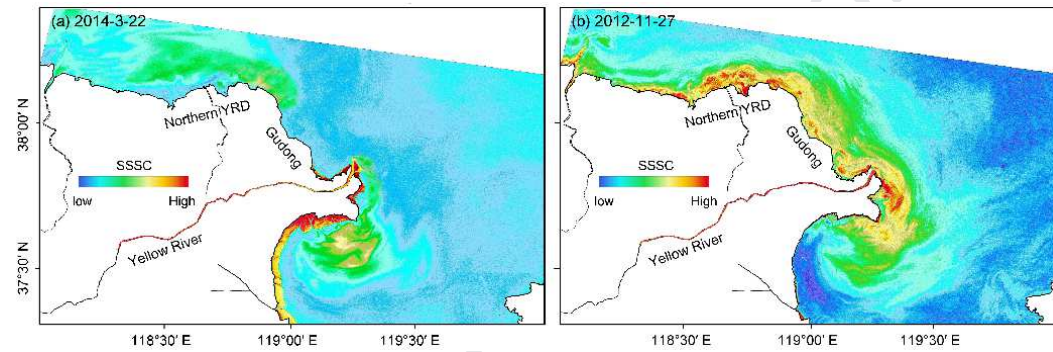
483 and formed the sediment plumes off the northern YRD and the river mouth.

484 Compared with the normal conditions, the ranges of high SSC area enlarge  
485 significantly under storm conditions (Fig. 12b). The maximum SSC off the northern  
486 YRD and the active river mouth was more than  $2.6 \text{ kg/m}^3$ . High SSC was profound  
487 off the Gudong coast, which was 3 times as large as that in normal conditions, with a  
488 maximum value of  $2.5 \text{ kg/m}^3$ , appearing at the most prominent point of Gudong dyke  
489 toward the sea. Off the river mouth, the weakened shear front and disappearance of  
490 low velocity zone were benefit for the sediment dispersal. Thus, the sediment plume  
491 of the river mouth diffuses to the central area of the Laizhou Bay, which causes high  
492 SSC appearing at this area.

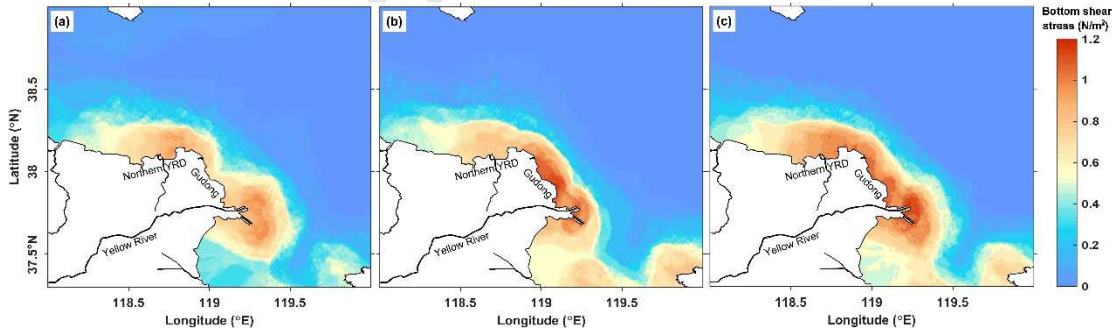
493 The characteristics of SSC distribution were related to the  $\tau_w$  and  $\tau_{cw}$  under  
494 storm conditions. The  $\tau_w$  was higher along the Gudong coast due to larger wave  
495 height, where its value reached approximately  $1.0 \text{ N/m}^2$  (Fig. 14b). The high value of  
496  $\tau_w$  at the river mouth was attributed to the shallow water of the mouth bar. In the most  
497 of the littoral area of YRD, the  $\tau_{cw}$  reached approximately  $1.1 \text{ N/m}^2$  (Fig. 14c), and  
498 the Gudong coast with larger values which was attributed to the higher  $\tau_w$  (Fig. 14b).  
499 This fact indicates that the high SSC along the Gudong coast is generated by local  
500 sediment resuspension in storm conditions. During storms, researchers found that the  
501 waves as an important agent in the reworking and retreat at the mud-rich deltas that  
502 are generally considered as either ‘river-dominated’, such as the Mississippi (Anthony,  
503 2015) or ‘tide-dominated’, such as the Chao Phraya (Uehara et al., 2010).



504

505 **Fig. 12.** The depth-averaged SSC: (a) in normal conditions; and (b) in storm conditions.

506

507 **Fig. 13.** Surface SSC (SSSC) retrieved from Landsat in the YRD region under: (a) in normal  
508 condition; and (b) under strong wind conditions.

509

510 **Fig.14.** Bottom shear stress (units:  $N/m^2$ ) in the littoral area of YRD: (a) current-induced; (b)  
511 wave-induced; and (c) total.512 

### 4.3.2 Sediment transport

513 In this section, the sediment transport characteristics were analyzed by  
514 calculating the residual transport of sediment ( $Tr_{sed}$ ) through a unit width, which can  
515 be defined as follows:

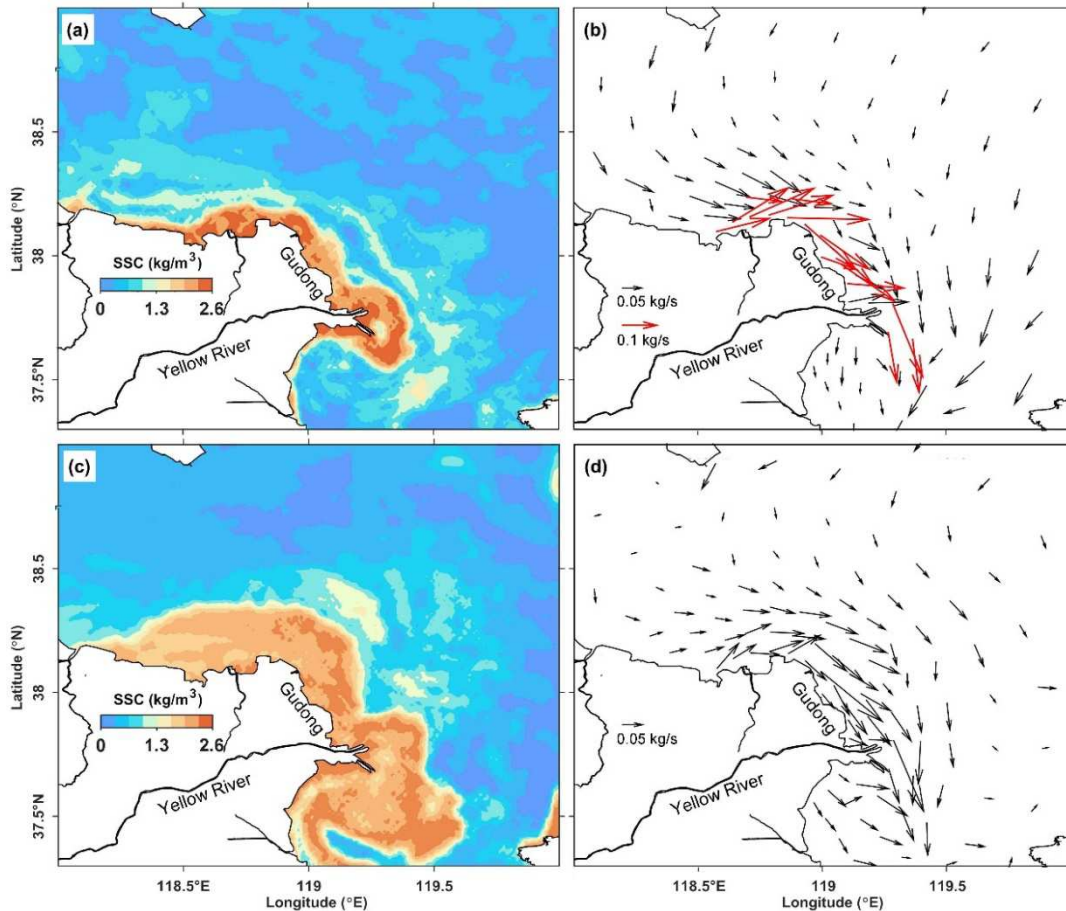
$$Tr_{sed} = \frac{1}{T} \int_0^T \int_{-H}^{\eta} \vec{V}(x, y, z, t) \cdot C(x, y, z, t) dt \quad (12)$$



516 where  $\eta$  is the surface elevation,  $H$  is the still water depth, and  $\vec{V}$  is the horizontal  
517 velocity vector,  $C$  is the sediment concentration, and  $T$  is the time period. As shown in  
518 Fig. 7, the whole process of the repeated storm lasted for nearly 50 hours. During the  
519 whole process, a wind turn occurred, forming two strong wind periods with different  
520 directions, i.e. the northeasterly wind period (NEP) and the northwesterly wind period  
521 (NWP). The dividing time of these two periods was approximately the middle time of  
522 the whole storm process, thus we can take 25 h as  $T$  to calculate  $Tr_{sed}$  of these two  
523 periods. The average SSC and residual of sediment transport rate are shown in Fig.  
524 15.

525 From Fig. 15, we can see that the NEP was the growth and duration of storm  
526 process with larger average wind speed, while the NWP showed a downward trend.  
527 Therefore, the NEP appeared a larger maximum value of than the NWP. Although the  
528 wind speed was weakening as a whole during the NWP, there was also a process of  
529 wind acceleration with a maximum wind speed of 18.0 m/s. During the process of  
530 offshore and southward transportation of sediment, a large amount of suspended  
531 sediment diffuses to the sea and Laizhou Bay. Therefore, during the NWP the area of  
532 high SSC was more widely distributed, and the area larger than  $1.5 \text{ kg/m}^3$  increased  
533 by nearly 50% compared with the NEP.





534  
 535 **Fig. 15.** The sediment transport features: (a) the suspended sediment concentrations and (b)  
 536 residual sediment mass transport during northeasterly wind; (c) the suspended sediment  
 537 concentrations and (d) residual sediment mass transport during northwesterly wind.

538 During the NEP, the residual transport of sediment increased with the decrease of  
 539 water depth. The larger value appeared off the Gudong coast, with the value of 0.23  
 540 kg/s. Although the residual transport of sediment during the NWP was less than that  
 541 during the NEP, it also showed a trend of increasing with the decrease of water depth,  
 542 with a high value of more than 0.18 kg/s off the Gudong coast and river mouth. The  
 543 directions of sediment transport were similar during these two periods, and basically  
 544 consistent with the direction of water transport. The main difference of them occurred  
 545 in the deep area, but the rates were mostly less than 0.05 kg/s. In both periods, the  
 546 sediment was transported offshore and southward as a whole. Specifically, the  
 547 sediment along the northern YRD coast was mainly transported eastward. After

548 arriving at the Gudong coast, sediment was transported southeast, and continued to  
549 transport to the central area of the Laizhou Bay after passing the river mouth.

550 Different from the offshore transport in the littoral area of YRD during storm  
551 surge, the sediment is transported landward by the storm surge in the Yangtze River  
552 submerged delta (Dai et al. 2015). Coastal geometry may account for this difference:  
553 compared with Bohai Bay and Laizhou Bay, the main coastline of the Yellow River  
554 Delta protrude toward the sea, which makes the storm energy easier to gather in its  
555 near shore; while the Yangtze River Delta is characterized as a channel-shoal system  
556 with multiple outlets and shallow shoals, and the sediment can be transported to the  
557 shore along the channel. Similarly, along the Ebro Delta coast (Spain) whose  
558 geometry is cusp, researchers found that future trends in sea level rise produce  
559 exacerbated cross-shore sediment transport by storm forcing (Grases et al. 2020).

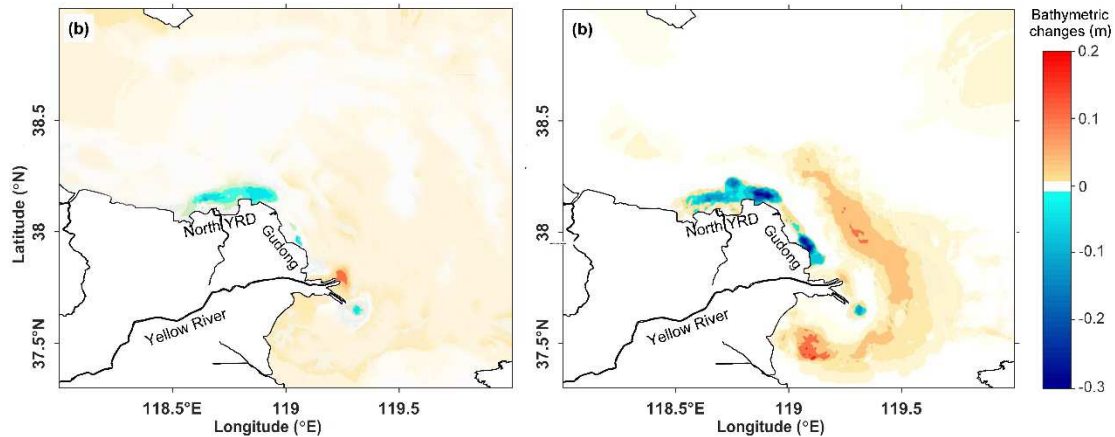
#### 560 **4.4 Seabed erosion**

561 Having identified the main directions and magnitudes of sediment transport, the  
562 resulting morphological changes due to the storm are investigated. The final  
563 bathymetric changes, obtained from Runs 1 and 2, are shown in Fig. 16a and Fig. 16b,  
564 respectively. Positive values hereafter represent accretion and negative values  
565 represent erosion. It can be seen that in most parts of the littoral area the bed level  
566 changed within the confines of -0.05 m to 0.05 m in normal conditions (Fig. 16a). The  
567 seabed erosion off Gudong was also slight due to its insignificant sediment transport.  
568 Whereas in storm conditions, the changing hydrodynamics and sediment transport  
569 induced significant nearshore erosion. Fig. 16b shows that the seabed erosion of the

570 Gudong and the northern YRD reached 0.1 m to 0.15 m, even more than 0.2 m near  
571 the dike area. While, the main siltation occurred in the central area of Laizhou Bay.  
572 Overall, the area (off the YRD, 118°E -120°E, 37.3°N -38°N) of seabed erosion in  
573 storm conditions was 362.67 km<sup>2</sup>, nearly 3 times as large as that in normal conditions,  
574 and the erosion volume is 0.0543 km<sup>3</sup>, about 20 times as large as that in normal  
575 conditions. Therefore, the seabed erosion caused by the changes of hydrodynamics  
576 and sediment transport under storm surge is an important factor in the coastal seabed  
577 erosion of the YRD.

578 In order to explore the seabed changes after the storm, the bathymetric changes  
579 during the recovery period after the storm were calculated. The time range of recovery  
580 period was determined according to the wind speed and direction observed in P2 site.  
581 As shown in Fig. 17, the end of this strong wind at 3:00 on April 15, indicating the  
582 recovery period began at this time. At the time of 22:00 on April 18, strong wind  
583 occurred again, indicating the recovery period began at this time and it lasted totaling  
584 91 hours. Similar to the SSC calculated in the normal conditions in experiment 1, the  
585 SSC off the north YRD and the active river mouth area was about 1.5 kg/m<sup>3</sup>, while in  
586 other areas it was less than 0.5 kg/m<sup>3</sup> (Fig. 18a). The residual transport of sediment  
587 through a unit width was also similar to that calculated in Experiment 1 in light wind  
588 conditions. There was no strong deposition or erosion area, and it was basically in the  
589 equilibrium state during recovery period (Fig.18b). Along Guong coast, which had  
590 been severely eroded during storm period, the bathymetry did not change significantly.  
591 It can be seen that it was difficult to recover the seabed erosion in the short term after

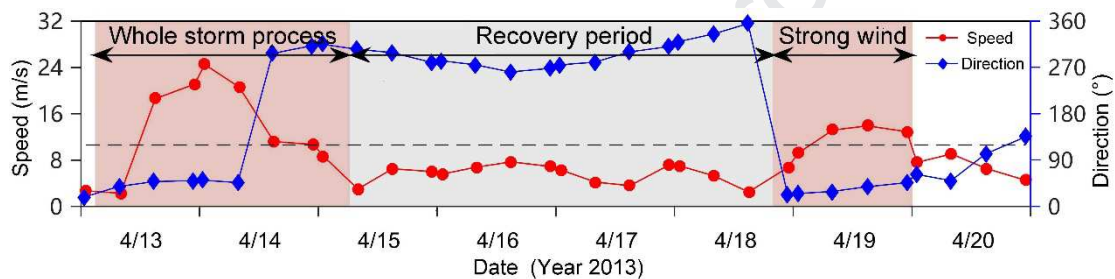
592 the storm, due to the insignificant sediment transport and deposition.



593

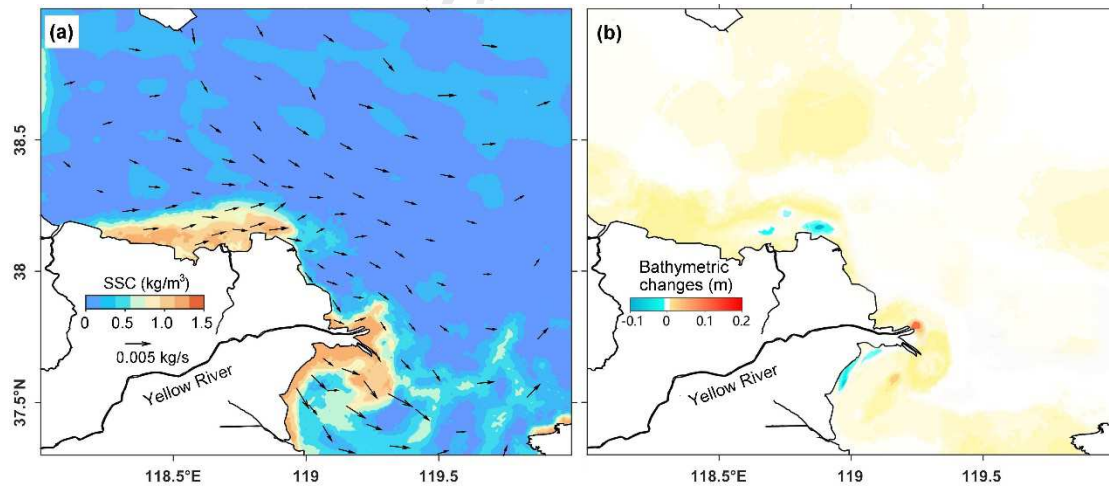
594 **Fig. 16.** Computed bathymetric changes (a) in normal conditions, and (b) in storm conditions.

595 Positive values represent accretion and negative values represent erosion.



596

597 **Fig. 17.** The changes of wind speed and direction during and after the storm.



598

599 **Fig. 18.** (a) Suspended sediment concentrations and residual sediment mass transport after the

600 storm; (b) erosion and accretion pattern after the storm.

#### 601 4.5 Frequency of strong wind

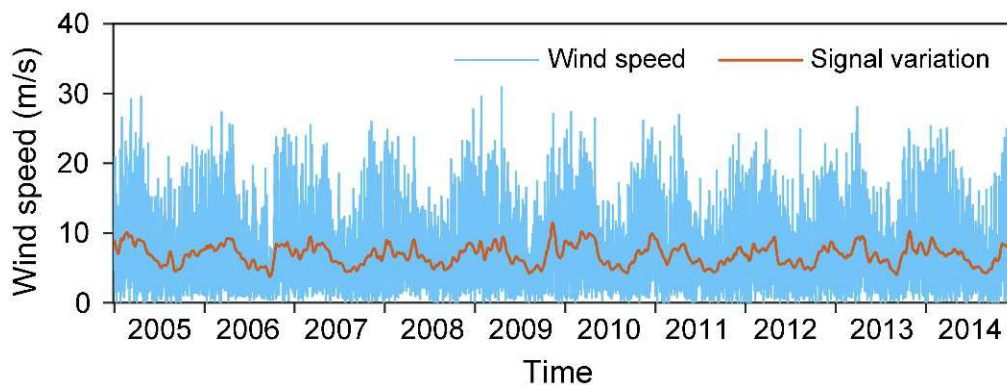
602 The northern YRD and the Gudong coast are abandoned delta lobes, which

603 underwent erosion after the river channel shifted southward. Despite of the coastal

604 defenses (dikes) being built, the overall coastal area continued to be in the state of

605 erosion and coastal managers were obliged to build protection works constantly, for  
 606 example the pipe pile projects outside the destroyed dikes in 2004 and in 2016.  
 607 Previous studies attributed the long term erosion to the avulsion of Yellow River and  
 608 subsequent lack of sediment supply (Li et al., 2000; Xing et al., 2016), while this short  
 609 timescale event hardly explain the long-term eroded states.

610 Although the winter storm surge is an extreme event, the storm-induced coast  
 611 erosion plays an important role in the coastal geomorphological changes of the YRD.  
 612 On the one hand, the effects of a storm give a distinguished interpretation for the  
 613 seabed erosion, and on the other hand, storms occur at a higher frequency. Based on  
 614 the hourly wind field data of P2 site from 2005 to 2014, the time series variation  
 615 process of wind speed is analyzed. As shown in Fig. 19, the wind speed series has  
 616 obvious seasonal variation characteristics. In winter and spring, the wind speeds are  
 617 larger, while in summer, the wind speed is smaller. From the monthly scale change  
 618 process of wind speed, the average probability of strong wind (speed more than 10.8  
 619 m/s) for 7 consecutive months from October to May of next year is 10.28%, the  
 620 maximum is 22.14%, which appears in February of 2009.

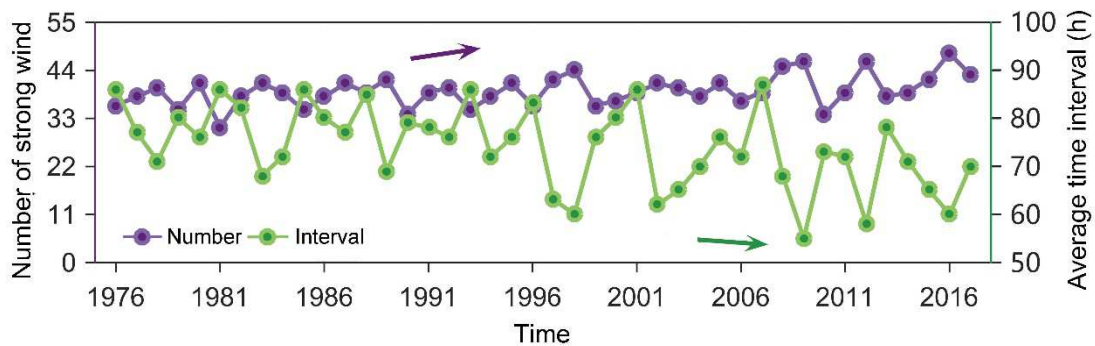


621  
 622 **Fig. 19.** Time series of observed wind speed and the signal variations in a monthly scale.

623 Using the ECMWF wind data, the frequency and interval time of strong wind in



624 autumn-winter-spring (October 15 to April 15 of next year) since 1976 can be  
 625 calculated. The results are shown in Fig. 20. Statistics show that the average number  
 626 of strong wind occurred 39 times per period, 31 times at least, from October 1981 to  
 627 May 1982, and 48 times at most, from October 2016 to May 2017. Since 1976, the  
 628 number of strong winds has fluctuated slightly upward, while the average time  
 629 interval of strong wind has fluctuated slightly downward. Thus, in the past 40 years,  
 630 the YRD has seen more frequent strong winds. This fact indicates that the erosion  
 631 state is mainly due to the accumulative effect of scour during storms, not merely  
 632 attributable to the frequent avulsion.



633  
 634 **Fig. 20.** Variation of the number of strong winds in autumn-winter-spring and the mean time  
 635 between two strong winds since 1976.

## 636 5 Conclusions

637 In this study, the effect of storms on the hydrodynamics and sediment transport  
 638 off the YRD were examined using a coupled modelling system including tides, waves,  
 639 and sediment processes. Verifications of flow field, wave heights, tides, sediment  
 640 concentrations demonstrated that the model can reproduce the hydrodynamic and  
 641 sediment processes and indicated storm erosion occurring in nearshore zones of the  
 642 northern YRD and Gudong.

643 The results of numerical experiments show that the interactions between the tide  
644 and wind-driven current during a storm period strengthen the residual currents and  
645 weaken the tidal shear front in the shallow areas. In addition to hydrodynamic  
646 changes, the strong northerly wind used in this numerical model causes the maximum  
647 wave heights of more than 2 m appearing at the Gudong coast. Under the influence of  
648 changing hydrodynamics during the storm, resuspension and sediment transport  
649 occurs, which leads to higher sediment concentration, with the maximum SSC  
650 exceeding  $2.5 \text{ kg/m}^3$  nearshore the northern YRD. The local resuspension due to  
651 greater wave-induced bottom stress promotes the sediment plume to shift to the  
652 Gudong coast. Besides, the sediment transported offshore and southward. The  
653 dynamic and sediment transport changes under storm conditions caused significant  
654 changes in seabed erosion and siltation. The area of seabed erosion area was nearly  
655 three times as large as that under normal conditions, and the erosion volume was  
656 nearly 20 times as large as that under normal conditions. No significant recovery after  
657 a storm and frequent strong winds have an accumulative effect on the seabed erosion.  
658 The results from this study improve our understanding of the formation mechanism of  
659 the eroded coast in the YRD: the accumulated storm erosion is more likely to  
660 dominate the long-term erosive coastal states, not just the frequent avulsion and of  
661 Yellow River and subsequent discontinuity of sediment supply.

## 662 **Acknowledgements**

663 The Landsat data used in this study are available at <https://glovis.usgs.gov>. Sea  
664 surface wind and atmospheric pressure data obtained from ECMWF are available at



665 <http://apps.ecmwf.int/datasets/>. Open ocean boundary tidal information included the  
666 major tide harmonic constituents is provided by the TPXO 7.2 Global Tidal Solution,  
667 at [http://volkov.oce.orst.edu/tides/tpxo8\\_atlas.html](http://volkov.oce.orst.edu/tides/tpxo8_atlas.html). The source code of the Delft3D  
668 model is freely available at <https://oss.deltares.nl/web/delft3d/source-code>. The field  
669 observation data and input files which are necessary to reproduce the experiments  
670 used in this study are available upon formal request to the correspondence author  
671 ([slchen@sklec.ecnu.edu.cn](mailto:slchen@sklec.ecnu.edu.cn)). This study was financially supported by the National  
672 Key Research and Development Program of China (No. 2017YFC0405503), the  
673 National Natural Science Foundation of China (No. U1706214) and the Open  
674 Research Fund of SKLEC (SKLEC-PGKF201903). The authors appreciate the two  
675 reviewers for their excellent comments and suggestions that improved this paper. We  
676 also acknowledge the editors for their assistance in editing the manuscript.

## 677 **References**

- 678 Allen, J.I., Somerfield, P.J., Gilbert, F.J., 2007. Quantifying uncertainty in high-resolution coupled  
679 hydrodynamic-ecosystem models. *Journal of Marine Systems* 64, 3-14.
- 680 Anthony, E.J., 2015. Wave influence in the construction, shaping and destruction of river deltas: A  
681 review. *Marine Geology* 361, 53-78.
- 682 Becker, M., Papa, F., Karpytchev, M., Delebecque, C., Krien, Y., Khan, J.U., Ballu, V., Durand, F.,  
683 Cozannet, G.L., Islam, A.K.M.S., Calmant, S., Shum, C.K., 2020. Water level changes,  
684 subsidence, and sea level rise in the Ganges-Brahmaputra-Meghna delta. *PNAS* 117(4),  
685 1867-1876.
- 686 Beihai Branch of State Oceanic Administration People's Republic of China. The northern China  
687 Marine Disasters Bulletin (2013) [EB/OL] <http://ncs.mnr.gov.cn/>. 2014-04-01.
- 688 Bi, N.S., Wang, H.J., Yang, Z.S., 2014. Recent changes in the erosion-accretion patterns of the  
689 active Huanghe (Yellow River) delta lobe caused by human activities. *Continental Shelf*

- 690 Research 90: 70-78.
- 691 Bian, S.H., Hu, Z., Liu, J., Zhu, Z., 2016. Sediment suspension and the dynamic mechanism  
692 during storms in the Yellow River Delta. *Environmental Monitoring & Assessment*, 189: 3.
- 693 Bjarnadottir, S. 2011. Social vulnerability index for coastal communities at risk to hurricane  
694 hazard and a changing climate. *Natural Hazards* 59, 1055-1075.
- 695 Blum, M.D., Roberts, H.H., 2009. Drowning of the Mississippi Delta due to insufficient sediment  
696 supply and global sea-level rise. *Nature Geoscience* 2, 488-491.
- 697 Boudet, L.F., Sabatier, F., Radakovitch, O., 2017. Modelling of sediment transport pattern in the  
698 mouth of the Rhone delta: Role of storm and food events. *Estuarine, Coastal and Shelf  
699 Science* 198, 568-582.
- 700 Brown, J.M., Ciavola, P., Masselink, G., Mccall, R., Plater, A.J., 2016. Preface: monitoring and  
701 modelling to guide coastal adaptation to extreme storm events in a changing climate. *Natural  
702 Hazards & Earth System Sciences* 16, 463-467.
- 703 Cao, Z.D., Lou, A.G., 2011. A three dimensional numerical simulation of the wind-driven  
704 circulation during winter in the Bohai Sea by FVCOM (in Chinese with English abstract).  
705 *Periodical of Ocean University of China*, 6787: 183-194
- 706 Chen, G., Niu, Y., Wen, S., Bao, C., Wu, B., Zhang, R., Gu, H., 1992. *Marine Atlas of Bohai Sea,  
707 Yellow Sea, East China Sea: Hydrology*. China Ocean Press, Beijing. p.523.
- 708 Chen, S., Zhang, G., Chen, X., 2006. Coastal erosion feature and mechanism at Feiyantan in the  
709 Yellow River delta. *Marine Science Bulletin* 8, 11-20.
- 710 Dai, Z.J., Fagherazzi, S., Mei, X.F., Gao, J.J., 2016. Decline in suspended sediment concentration  
711 delivered by the Changjiang (Yangtze) River into the East China Sea between 1956 and 2013.  
712 *Geomorphology* 268, 123-132.
- 713 Dou, G.R., 1999. Incipient motion of coarse and Fine sediment (in Chinese, with English abstract).  
714 *Journal of Sediment Research* 6, 1-9.
- 715 Edmonds, D.A., Slingerland, R.L., 2010. Significant effect of sediment cohesion on delta  
716 morphology. *Nature Geoscience* 3, 105-109.
- 717 Fan, Y.S., Chen, S.L., Zhao, B., Pan, S., Jiang, C., Ji, H.Y., 2018. Shoreline dynamics of the active  
718 Yellow River delta since the implementation of Water-Sediment Regulation Scheme: a  
719 remote-sensing and statistics-based approach. *Estuarine, Coastal and Shelf Science* 200,

- 720 406-419.
- 721 Florin, I.Z., Florin, T., Nikolay, N.V., Alfred, V.S., 2017. Storm climate on the Danube delta coast:  
722 evidence of recent storminess change and links with large-scale teleconnection patterns.  
723 *Natural Hazards* 87, 1-23.
- 724 Goff, J.A., Allison, M.A., Gulick, S.P.S., 2010. Offshore transport of sediment during cyclonic  
725 storms: Hurricane Ike (2008), Texas Gulf Coast, USA. *Geology* 38, 351–354.
- 726 Gong, W., Jia, L., Shen, J., Liu, J.T., 2014. Sediment transport in response to changes in river  
727 discharge and tidal mixing in a funnel-shaped micro-tidal estuary. *Continental Shelf Research*  
728 76, 89-107.
- 729 Grant, W.D., Madsen, O.S., 1979. Combined wave and current interaction with a rough bottom.  
730 *Journal of Geophysical Research* 84, 1797-1808.
- 731 Grases, A., Gracia, V., García-León, M., Jue, L.Y., Sierra, J.P., 2020. Coastal flooding and erosion  
732 under a changing climate: Implications at a low-lying coast (Ebro Delta). *Water* 12, 346.
- 733 Hao, Y., Le, K.T., Liu, X.Q., 2010. A numerical prediction of the tidal characteristics in 2010 of  
734 Yellow River Delta (in Chinese, with English abstract). *Chinese Marine Science* 24, 43-46.
- 735 Huang, D., 1995. Modeling Studies of Barotropic and Baroclinic Dynamics in the Bohai Sea.  
736 Ph.D Thesis. Hamburg, Germany: Hamburg University.
- 737 Huang, D.J., Chen, Z.Y., Su, J.L., 1996. Application of three-dimensional shelf sea model in the  
738 Bohai Sea: I. tidal current, wind-driven current and their interaction (in Chinese, with English  
739 abstract). *Aeta Oceanologia Sinica* 18, 1-15.
- 740 Jiang, C., Pan, S., Chen, S.L., 2017. Recent morphological changes of the Yellow River (Huanghe)  
741 submerged delta: causes and environmental implications. *Geomorphology* 293, 93-107.
- 742 Kong, D., Miao, C., Borthwick, A.G.L., Duan, Q.Y., Liu, H., Sun, Q.H., Ye, A.Z., Di, Z.H., Gong  
743 W., 2015. Evolution of the Yellow River delta and its relationship with runoff and sediment  
744 load from 1983 to 2011. *Journal of Hydrology* 520, 157-167.
- 745 Uehara, K., Pramot, S., Yoshiki, S., Thanawat, J., 2010. Erosion and accretion processes in a  
746 muddy dissipative coast, the Chao Phraya River delta, Thailand. *Earth Surface Processes and*  
747 *Landforms* 35(14), 1701-1711.
- 748 Kuenzer, C., Ottinger, M., Liu, G.H., Sun, B., Baumhauer, R., Dech, S., 2014. Earth observation  
749 based coastal zone monitoring of the Yellow River delta: dynamics in China's second largest

- 750 oil producing region observed over four decades. *Applied Geography* 55, 92-107.
- 751 Li, G.X., Cheng, G., Wei, H., Pan, W., Ren, Y., Ding, D., Zhou, Y., Zhao, J., 1994. Tidal shear  
752 front off modern Yellow River mouth. *Chinese Science Bulletin* 39, 928–932.
- 753 Li, G.X., Zhuang, K., Wei, H., 2000. Sedimentation in the Yellow River delta. Part III. Seabed  
754 erosion and diapirism in the abandoned subaqueous delta lobe. *Marine Geology* 168,  
755 129-144.
- 756 Li, Y., Tian, L.Z., Pei, Y.D., Wang, F., Wang, H., 2016. Numerical simulation of storm surge  
757 inundation in the west zone of Bohai Bay. *Geological Bulletin of China* 35(10), 1638-1645.
- 758 Liu, F., Chen, H., Cai, H., Luo, X., Ou, S., Yang, Q., 2017. Impacts of ENSO on multi-scale  
759 variations in sediment discharge from the Pearl River to the South China Sea.  
760 *Geomorphology* 293, 24-36.
- 761 Liu, F., Xie, R., Luo, X., Yang, L., Cai, H., Yang, Q., 2019. Stepwise adjustment of deltaic  
762 channels in response to human interventions and its hydrological implications for sustainable  
763 water managements in the Pearl River Delta, China. *Journal of Hydrology* 573, 194-206.
- 764 Liang, B.C., Li, H.J., 2008. Bottom shear stress under wave-current interaction. *Journal of*  
765 *Hydrodynamics Series B* 20, 88-95.
- 766 Lu, J., Qiao, F.L., Wang, X.H., Wang, Y.G., Teng, Y., Xia, C.S., 2011. A numerical study of  
767 transport dynamics and seasonal variability of the Yellow River sediment in the Bohai and  
768 Yellow Seas. *Estuarine Coastal and Shelf Science* 95, 39-51
- 769 Luo, Z., Zhu, J., Wu, H., Li, X., 2017. Dynamics of the sediment plume over the Yangtze Bank in  
770 the Yellow and East China Seas. *Journal of Geophysical Research Oceans* 122, 10073-10090.
- 771 Lv, X., Yuan, D., Ma, X., Tao, J., 2014. Wave characteristics analysis in Bohai Sea based on  
772 ECMWF wind field. *Ocean Engineering* 91, 159-171.
- 773 Martin, J., Sheets, B., Paola, C., Hoyal, D., 2009. Influence of steady base-level rise on channel  
774 mobility, shoreline migration, and scaling properties of a cohesive experimental delta. *Journal*  
775 *of Geophysical Research Earth Surface* 114, F03017.
- 776 Milly, P.C., Wetherald, R.T., Dunne, K.A., Delworth, T.L., 2002. Increasing risk of great floods in  
777 a changing climate. *Nature* 415, 514-517.
- 778 Murray, N.J., Phinn, S.R., DeWitt, M., 2019. The global distribution and trajectory of tidal flats.  
779 *Nature* 565, 222-225.

- 780 Nicholls R.J., Cazenavem, A., 2010. Sea-level rise and its impact on coastal zones. *Science* 328,  
781 1517.
- 782 Pelling, H.E., Uehara, K., Green, J.A.M., 2013. The impact of rapid coastline changes and sea  
783 level rise on the tides in the Bohai Sea, China. *Journal of Geophysical Research: Oceans* 118,  
784 3462-3472.
- 785 Qi, S., Liu, H., 2017. Natural and anthropogenic hazards in the Yellow River Delta, China. *Natural*  
786 *Hazards* 85, 1-5
- 787 Qiao, L.L., Bao, X.W., Wu, D.X., Wang, X.H., 2008. Numerical study of generation of the tidal  
788 shear front off the Yellow River mouth. *Continental Shelf Research* 28, 1782-1790.
- 789 Quan, Y.Z., 2014. Numerical simulation of sediment movement and its dynamic mechanism in a  
790 strong wind processed of northern sea of the Yellow River Delta. Doctoral Dissertation.  
791 Qingdao, China: Ocean University of China.
- 792 Ralston, D.K., Geyer, R., Lerczak, J.A., 2010. Structure, variability, and salt flux in a strongly  
793 forced salt wedge estuary. *Journal of Geophysical Research: Oceans* 115, C06005.
- 794 Ralston, D.K., Warner, J.C., Geyer, W.R., Wall, G.R., 2013. Sediment transport due to extreme  
795 events: the Hudson River estuary after tropical storms Irene and Lee. *Geophysical Research*  
796 *Letters* 40, 5451-5455.
- 797 Reitz, M.D., Jerolmack, D.J., 2012. Experimental alluvial fan evolution: Channel dynamics,  
798 slope controls, and shoreline growth. *Journal of Geophysical Research: Earth Surface* 117,  
799 F02021.
- 800 Ren, R., Chen, S.L., Dong, P., Liu, F., 2012. Spatial and temporal variations in grain size of  
801 surface sediments in the littoral area of Yellow River delta. *Journal of Coastal Research* 28,  
802 44-53.
- 803 Shi, W., Wang, M., Jiang, L., 2011. Spring-neap tidal effects on satellite ocean color observations  
804 in the Bohai Sea, Yellow Sea, and East China Sea. *Journal of Geophysical Research* 116:  
805 C12032.
- 806 Signell, R.P., Beardsley, R.C., Graber, H.C., Capotondi, A., 1990. Effect of wave-current  
807 interaction on wind-driven circulation in narrow, shallow embayments. *Journal of*  
808 *Geophysical Research* 95, 9671-9678.
- 809 Syvitski, J.P.M., Kettner, A., 2011. Sediment flux and the Anthropocene. *Philosophical*

- 810 Transactions of the Royal Society A: Mathematical, Physical and Engineering Sciences 369,  
811 957-975.
- 812 Tessler, Z.D., Vorosmarty, C.J., Grossberg, M., et al., 2015. Profiling risk and sustainability in  
813 coastal deltas of the world. *Science* 349, 638-643.
- 814 Vaz, N., Dias, J.M., 2014. Residual currents and transport pathways in the Tagus estuary, Portugal:  
815 the role of freshwater discharge and wind. *Journal of Coastal Research* 70, 610-615.
- 816 Van Rijn, L.C., 1993. Principles of sediment transport in river, estuaries and coastal seas. AQUA  
817 Publications, the Netherlands, p.535.
- 818 Wang, H., Bi, N., Saito, Y., Wang, Y., Sun, X., Zhang, J., Yang, Z., 2010. Recent changes in  
819 sediment delivery by the Huanghe (Yellow River) to the sea: causes and environmental  
820 implications in its estuary. *Journal of Hydrology* 391, 302-313.
- 821 Wang, H., Saito, Y., Zhang, Y., Bi, N., Sun, X., Yang, Z., 2011. Recent changes of sediment flux to  
822 the western Pacific Ocean from major rivers in East and Southeast Asia. *Earth-Science*  
823 *Reviews* 108, 80-100.
- 824 Wang, H., Wang, A., Bi, N., Zeng, X., Xiao, H., 2014. Seasonal distribution of suspended  
825 sediment in the Bohai Sea, China. *Continental Shelf Research* 90, 17-32.
- 826 Wang, H., Yang, Z., Li, Y., Guo, Z., Sun, X., Wang, Y., 2007. Dispersal pattern of suspended  
827 sediment in the shear frontal zone off the Huanghe (Yellow River) mouth. *Continental Shelf*  
828 *Research* 27, 854-871.
- 829 Wang, N., Li, G., Qiao, L., Shi, J., Dong, P., Xu, J., Ma, Y., 2017. Long-term evolution in the  
830 location, propagation, and magnitude of the tidal shear front off the Yellow River mouth.  
831 *Continental Shelf Research* 137, 1-12.
- 832 Warner, J.C., Sherwood, C.R., Signell, R.P., Harris, C.K., Arango, H.G., 2008. Development of a  
833 three-dimensional, regional, coupled wave, current, and sediment-transport model.  
834 *Computers & Geosciences* 34, 1284-1306.
- 835 Winterwerp, J.C., Maa, J., Sanford, L., Schoellhamer, D., 2007. On the sedimentation rate of  
836 cohesive sediment. In: *Estuarine and Coastal Fine Sediments Dynamics INTERCOH 2003*.  
837 Elsevier, p. 209-226.
- 838 Wolters, M.L., Kuenzer, C., 2015. Vulnerability assessments of coastal river deltas-categorization  
839 and review. *Journal of Coastal Conservation* 19, 345-368.

- 840 Wu, X., Bi, N., Xu, J., Nittrouer, J.A., Yang, Z., Saito, Y., Wang, H., 2017. Stepwise  
841 morphological evolution of the active Yellow River (Huanghe) delta lobe (1976–2013):  
842 dominant roles of riverine discharge and sediment grain size. *Geomorphology* 292, 115-127.
- 843 Wu, X., Bi, N., Yuan, P., Li, S., Wang, H., 2015. Sediment dispersal and accumulation off the  
844 present Huanghe (Yellow River) delta as impacted by the Water-Sediment Regulation  
845 Scheme. *Continental Shelf Research* 111, 126-138.
- 846 Xing, F., Wang, Y.P., Wang, H.V. 2012. Tidal hydrodynamics and fine-grained sediment transport  
847 on the radial sand ridge system in the southern Yellow Sea. *Marine Geology* 291-294,  
848 192-210.
- 849 Xing, G., Wang, H., Yang, Z., Bi, N., 2016. Spatial and temporal variation in erosion and  
850 accumulation of the subaqueous Yellow River delta (1976–2004). *Journal of Coastal*  
851 *Research* 74, 32-47.
- 852 Xu, C., Gu, S., Liu, Z., Zhang, N., Yu, L., 2016. Characteristics of the river mouth bar in the past  
853 14 years of the Yellow River Water-Sediment Regulation (in Chinese, with English abstract).  
854 *Yellow River* 38, 69-73.
- 855 Yang, S., Milliman, J.D., Li, P., Xu, K., 2011a. 50,000 dams later: erosion of the Yangtze River  
856 and its delta. *Global and Planetary Change* 75, 14-20.
- 857 Yang, Z., Ji, Y., Bi, N., Lei, K., Wang, H., 2011b. Sediment transport off the Huanghe (Yellow  
858 River) delta and in the adjacent Bohai Sea in winter and seasonal comparison. *Estuarine*  
859 *Coastal and Shelf Science* 93, 173-181.
- 860 Ying, M., Li, J.F., Chen, S.L., Dai, Z.J., 2008. Dynamics characteristics and topographic profile  
861 shaping process of Feiyan Shoal at the Yellow River delta. *Marine Science Bulletin* 10,  
862 74-88.
- 863 Yuan, D., Zhu, J., Li, C., Hu, D., 2008. Cross-shelf circulation in the Yellow and East China Seas  
864 indicated by MODIS satellite observations. *Journal of Marine Systems* 70, 134-149.
- 865 Zhang, M., Dong, Q., Cui, T., Xue, C., Zhang, S., 2014. Suspended sediment monitoring and  
866 assessment for Yellow River estuary from Landsat TM and ETM+ imagery. *Remote Sensing*  
867 *of Environment* 146, 136-147.
- 868 Zhang, Y., 2011. Coastal environmental monitoring using remotely sensed data and GIS  
869 techniques in the modern Yellow River delta, China. *Environmental Monitoring &*



Journal Pre-proof

## Highlights

- Storm-induced energetic hydrodynamic forces intensify sediment resuspension and dispersal significantly.
- Wave-induced bottom stress promotes sediment plume and enhances local resuspension.
- Storms increase suspended sediment concentration and offshore sediment transport.
- Storm-induced accumulative effect on seabed scour tends to cause long-term erosion.

## **Conflict of interest**

The authors declared that they have no conflicts of interest to this work. We declare that we do not have any commercial or associative interest that represents a conflict of interest in connection with the work submitted.

Journal Pre-proof